SIAM J. SCI. COMPUT.
Vol. 31, No. 3, pp. 2231–2257

A CONSERVATIVE DISCONTINUOUS GALERKIN SEMI-IMPLICIT FORMULATION FOR THE NAVIER–STOKES EQUATIONS IN NONHYDROSTATIC MESOSCALE MODELING*

MARCO RESTELLI† AND FRANCIS X. GIRALDO‡

Abstract. A discontinuous Galerkin (DG) finite element formulation is proposed for the solution of the compressible Navier–Stokes equations for a vertically stratified fluid, which are of interest in mesoscale nonhydrostatic atmospheric modeling. The resulting scheme naturally ensures conservation of mass, momentum, and energy. A semi-implicit time-integration approach is adopted to improve the efficiency of the scheme with respect to the explicit Runge–Kutta time integration strategies usually employed in the context of DG formulations. A method is also presented to reformulate the resulting linear system as a pseudo-Helmholtz problem. In doing this, we obtain a DG discretization closely related to those proposed for the solution of elliptic problems, and we show how to take advantage of the numerical integration rules (required in all DG methods for the area and flux integrals) to increase the efficiency of the solution algorithm. The resulting numerical formulation is then validated on a collection of classical two-dimensional test cases, including density driven flows and mountain wave simulations. The performance analysis shows that the semi-implicit method is, indeed, superior to explicit methods and that the pseudo-Helmholtz formulation yields further efficiency improvements.

Key words. compressible flows, Euler equations, Navier–Stokes equations, discontinuous Galerkin finite element method, nonhydrostatic model, semi-implicit time discretizations

AMS subject classifications. 65M60, 65M70, 35L65, 86A10

DOI. 10.1137/070708470

1. Introduction.

In recent years, great attention has been devoted to the discontinuous Galerkin (DG) finite element method in the context of geophysical fluid dynamics applications. This is motivated by the fact that the DG framework simultaneously provides a high-order discretization, great flexibility in the choice of the computational grid, discrete balance relations, robustness with respect to unphysical oscillations, and compact computational stencils which are a key element in order to exploit distributed-memory parallel computers with up to tens of thousands of processors. Without attempting to provide a complete review of the literature, we mention here [47, 2, 30, 39, 34, 32], where DG shallow water models are presented. The application of the DG method to compressible, nonhydrostatic atmospheric flows, using the Navier–Stokes equations or, when the flow is assumed to be inviscid, the Euler equations, is then considered in [31], where it is shown that the method represents a good candidate for the development of numerical climate and weather models. In the present paper, we continue the study initiated in [31] by focusing on the aspect of the time discretization which is, in fact, the most penalizing drawback of the DG method due to its high computational cost. This latter cost stems from the following

*Received by the editors November 17, 2007; accepted for publication (in revised form) December 29, 2008; published electronically May 7, 2009.
http://www.siam.org/journals/sisc/31-3/70847.html

†Ozean im Erdsystem, Max–Planck–Institut für Meteorologie, Bundesstraße 53, 20146 Hamburg, Germany (marco.restelli@zmaw.de). The work of this author is supported by MetStröm project of the Deutsche Forschungsgemeinschaft and the Office of Naval Research through the Visiting Scientist Program grant N00014-06-1-4023.

‡Department of Applied Mathematics, Naval Postgraduate School, Monterey, CA 93943 (fxgirald@nps.edu). The work of this author is supported by Office of Naval Research through program element PE-0602435N.

reasons: the need of a complete independent set of points for each element to span the local polynomial space; a stricter time-step than in continuous methods due to the upwinding mechanism in the numerical flux; and the fact that all previous applications have been confined to explicit time-integration. Our goal is to remedy the last two points. More precisely, the main purpose of this article is to show that it is possible to use a semi-implicit (SI) time-stepping method in combination with a DG spatial discretization, thus, improving the computational efficiency with respect to the explicit time discretization approach, without affecting the positive features of the method. The idea of numerically integrating in time a differential equation by using an explicit treatment for the nonstiff component and an implicit treatment for the stiff component, thus, obtaining a method which can be generally classified as "semi-implicit", is very general and has been exploited in different contexts, where correspondingly different criteria have been used to identify the stiff terms. In the context of geophysical fluid dynamics, the SI approach was first introduced in [38] for the solution of the primitive hydrostatic equations, where the stiff component was identified with the terms responsible for the gravity waves. Modifications were proposed in [10] for the hydrostatic case and the technique was then extended to the complete nonhydrostatic Euler equations in [53, 18, 52], with implicit treatment of both acoustic and gravity waves. Since then, the method has been widely employed in climate and weather prediction models, and we refer to [43, 7, 33] for further details. To our knowledge, this type of SI time discretization has never been used in combination with a DG spatial discretization, and the SI-DG formulation described in the present paper represents a novel contribution. This formulation, moreover, besides being suited for atmospheric flow problems, may be useful also in the context of smaller scale, low Mach number fluid dynamics simulations.

We notice here that a SI time discretization combined with a DG space discretization has been considered in [56, 55] for scalar equations with higher order derivatives, where the stiffness is due to the presence of the high order terms, and in [23, 26, 27] for the Navier–Stokes equations. Concerning this latter formulation, we observe that it is different from the one we propose in the present article. The method originally developed by Dolejší and Feistauer in [23] relies on a careful handling of the nonlinear problem arising from a fully implicit time-stepping strategy, and a key ingredient of the method is the choice of a particular numerical flux. This approach, thus, allows the use of large time-steps regardless of the Mach number. On the contrary, in our approach only the terms responsible for acoustic and gravity waves are treated implicitly, and there is much freedom in the choice of the numerical flux. As a result, the scheme we propose is less restrictive in regards to the numerical flux and is suitable for the treatment of low Mach number flows, where it results in a simpler implicit problem than [23] since the advective contributions are absent.

A final comment is in order concerning the solution algorithm for the linear system associated with the SI time discretization. In the present paper, we show that it is possible to reformulate such a system as a pseudo-Helmholtz problem for the sole pressure variable, the discretization of which is closely related to the local discontinuous Galerkin (LDG) methods proposed in [13, 3] for elliptic problems. By doing this, the number of unknowns is reduced by a factor four (and the resulting matrix problem by a factor of 16), since the sole pressure variable appears in the linear system rather than the complete set of degrees of freedom composed by density, horizontal and vertical velocities, and total energy. Due to this reduction in the size of the implicit system, the reformulation as a pseudo-Helmholtz problem yields a significant efficiency improvement compared to the solution of the original system.

An outline of the paper is as follows. In section 2 the governing equations are introduced. Section 3 deals with the SI time discretization, while the DG spatial discretization is presented in section 4. The space-time fully discretized problem is then summarized in section 5. In particular, a method to reformulate the resulting linear system as a pseudo-Helmholtz problem is described in section 5.2. The numerical validation of the proposed formulation is presented in section 6. Finally, conclusions and future developments are discussed in section 7.

2. Governing equations. In this section, we introduce the continuous equations representing the mathematical model for the atmospheric flow problem considered in the present paper. Various alternative equation sets have been proposed in the literature to describe the nonhydrostatic flow of a dry, stratified atmosphere. In [31] three different equation sets are examined by comparing the results of five spectral element and discontinuous Galerkin codes, and it is found that the conservative Navier–Stokes equations using density, momentum, and total energy as prognostic variables represent one of the most effective choices as far as accuracy is concerned. In addition, the fact that such an equation set is in conservation form, even when taking into account viscous stresses, makes it a suitable starting point for the construction of a numerical scheme endowed with discrete conservation properties. For these reasons, this equation set is considered in the present work. Restricting ourselves for simplicity to a two-dimensional case in the vertical (x, z) plane, and neglecting the Coriolis terms, we obtain the following system (see [5]):

$$\frac{\partial \mathbf{q}}{\partial t} + \nabla \cdot \mathcal{F}^e(\mathbf{q}) - \nabla \cdot \mathcal{F}^v(\mathbf{q}, \nabla \mathbf{q}) = \mathbf{G}(\mathbf{q}), \tag{2.1}$$

where each term is defined as follows: $\mathbf{q} = (\rho, \mathbf{V}^T, E)^T$ are the conserved quantities, ρ is the density, and, letting $\mathbf{v}$ denote the velocity field, c_v and g denote the specific heat for constant volume and the gravitational constant, respectively, T denote the temperature and $e = c_v T + \frac{1}{2}\mathbf{v} \cdot \mathbf{v} + gz$ represent the total energy, $\mathbf{V} = \rho \mathbf{v}$ is the momentum and $E = \rho e$ is the energy density. The inviscid and viscous fluxes and the source term in (2.1) are given by

$$\mathcal{F}^e(\mathbf{q}) = \begin{Bmatrix} \mathbf{V} \\ \frac{1}{\rho}\mathbf{V} \otimes \mathbf{V} + p\mathcal{I} \\ \frac{1}{\rho} H \mathbf{V} \end{Bmatrix}, \quad \mathcal{F}^v(\mathbf{q}, \nabla \mathbf{q}) = \begin{Bmatrix} 0 \\ \mathcal{F}^v_{\mathbf{V}}(\mathbf{q}, \nabla \mathbf{q}) \\ \mathbf{F}^v_E(\mathbf{q}, \nabla \mathbf{q}) \end{Bmatrix}, \quad \mathbf{G}(\mathbf{q}) = \begin{Bmatrix} 0 \\ \rho \mathbf{g} \\ 0 \end{Bmatrix},$$

where p is the pressure, $\mathbf{g} = -g\mathbf{k}$, with $\mathbf{k} = (0, 1)^T$, $H = E + p$ is the enthalpy, and the viscous fluxes are defined as

$$\mathcal{F}^v_{\mathbf{V}} = \mu \left[\nabla \mathbf{v} + \nabla \mathbf{v}^T + \lambda \nabla \cdot \mathbf{v} \mathcal{I} \right], \qquad \mathbf{F}^v_E = \frac{\mu c_p}{Pr} \nabla T + \mathbf{v} \cdot \mathcal{F}^v_{\mathbf{V}},$$

μ and λ denoting the two viscosity coefficients, c_p denoting the specific heat for constant pressure, and Pr being the Prandtl number. Using the Stokes hypothesis, we can set $\lambda = -\frac{2}{3}$. Notice that, although for practical applications a turbulence closure relation has to be considered to define the viscosity coefficients, in the present work we assume that these latter are known constants. Closure of system (2.1) is obtained through the equation of state, which, in terms of the solution variables, is written as

$$p = \frac{R}{c_v} \left(E - \frac{1}{2} \frac{V^2}{\rho} - \rho g z \right), \tag{2.2}$$

with $R = c_p - c_v$. Equation (2.1) reduces to the Euler equations when $\mu = 0$.

When solving system (2.1) for atmospheric flows, it can be expected that the flow is nearly hydrostatic, i.e., in the vertical momentum equation the two terms $\frac{\partial p}{\partial z}$ (from the inviscid flux) and ρg (from the source term) are much larger than the remaining ones. This can cause instabilities in the numerical approximation of the problem, due to cancellation of significant digits. To avoid this effect, problem (2.1) is usually reformulated in terms of deviations from a constant-in-time reference state (see [25] and, for an alternative, more sophisticated approach, [8]). Thus, we introduce $\overline{\mathbf{q}} = (\overline{\rho}, \overline{\mathbf{V}}^T, \overline{E})^T$ and $\overline{p} = p(\overline{\rho}, \overline{\mathbf{V}}, \overline{E})$ such that $\overline{\mathbf{V}} = 0$, $\frac{\partial \overline{p}}{\partial x} = 0$, $\frac{\partial \overline{E}}{\partial x} = 0$ (also implying $\frac{\partial \overline{p}}{\partial x} = 0$), and

$$\frac{d\overline{p}}{dz} = -\overline{\rho}\, g. \tag{2.3}$$

Upon defining $\mathbf{q}' = \mathbf{q} - \overline{\mathbf{q}}$ and $p' = p - \overline{p}$, we obtain

$$\frac{\partial \mathbf{q}'}{\partial t} + \nabla \cdot \mathcal{F}^{e\prime}(\mathbf{q}) - \nabla \cdot \mathcal{F}^{v}(\mathbf{q}, \nabla \mathbf{q}) = \mathbf{G}(\mathbf{q}'), \tag{2.4}$$

where

$$\mathcal{F}^{e\prime}(\mathbf{q}) = \left\{ \begin{array}{c} \mathbf{V} \\ \frac{1}{\rho}\mathbf{V} \otimes \mathbf{V} + p'\mathcal{I} \\ \frac{1}{\rho} H \mathbf{V} \end{array} \right\}.$$

Equation (2.2) allows for an expression of p' which is independent from $\overline{\rho}$, $\overline{E}$

$$p' = \frac{R}{c_v}\left(E' - \frac{1}{2}\frac{V^2}{\rho} - \rho' g z\right),$$

so that no cancellation problems occur in evaluating the pressure perturbation. Problem (2.4) has the advantage that all the terms in the vertical momentum equations are of the same order of magnitude. For this reason, in the following we will always use (2.4) instead of (2.1), and we will drop the primes for simplicity.

2.1. Treatment of the open boundary conditions. In practical applications, it is usually necessary to truncate the computational domain with artificial boundaries, not corresponding to any physical entity. Ideally, an "open boundary" condition is desired on these boundaries, avoiding any reflection of outgoing signals. A simple and robust solution is represented by an *absorbing layer*, also known as a *sponge layer*, as discussed in [36, 24]. In these references, a method is described to optimize the structure of the absorbing layer in the case where the primitive variable formulation is considered, i.e., when the prognostic variables are Exner pressure, velocity, and potential temperature. To apply these results to the conservative formulation (2.4), we can in principle perform a change of variables from conservative to primitive variables, apply the damping coefficients, and then transform back to conservative variables. In practice, this can be done as follows: denoting by $\mathbf{q}_b = (\rho_b, \mathbf{V}_b^T, E_b)^T$ a known boundary datum, we modify system (2.4) to obtain

$$\frac{\partial \mathbf{q}}{\partial t} = \mathscr{S}^{NS}(\mathbf{q}) - T^{cv}\left(\mathbf{q} - \mathbf{q}_b\right), \tag{2.5}$$

with $\mathscr{S}^{NS}(\mathbf{q}) = -\nabla \cdot \mathcal{F}^{e}(\mathbf{q}) + \nabla \cdot \mathcal{F}^{v}(\mathbf{q}, \nabla \mathbf{q}) + \mathbf{G}(\mathbf{q})$ and

$$T^{cv} = M^{-1} T^{pv} M. \tag{2.6}$$

In (2.6), M is a 4×4 matrix representing the linearized transformation between conservative variables and primitive variables, the linearization being performed in a

neighborhood of $\mathbf{q}_b$, while T^{pv} is a diagonal matrix whose four entries are computed as in [36, 24]. Once the absorbing layer has been introduced within the computational domain, the particular boundary condition prescribed on the boundary of the computational domain itself has in practice no effect on the computed solution, so that, because of the ease of implementation, we impose the Dirichlet condition $\mathbf{q} = \mathbf{q}_b$. We notice that, although introducing an absorbing layer is a common solution to handle nonreflecting boundary conditions, more sophisticated alternatives are possible. In particular, we are currently exploring Higdon-type high-order boundary conditions [20, 22, 21] which we reserve for future work since this topic is beyond the scope of the present paper.

2.2. Identification of the fast waves in the model. In order to devise a semi-implicit time-integration scheme for (2.4), it is first necessary to identify the terms responsible for the fastest waves in the model, i.e., acoustic and gravity waves. In fact, in the semi-implicit time-integration procedure, an implicit treatment will be selectively applied to such terms, while an explicit approach will be adopted for the remaining ones. Following [37], we identify these terms as the divergence of the mass flux in the continuity equation, the pressure gradient and the buoyancy term in the momentum equation and the divergence of the enthalpy flux in the energy equation (see also the simplified stability analysis in [42]). To linearize these terms, we introduce the linear operator

$$\mathscr{L}^{NS}(\mathbf{q}) = -\nabla \cdot \mathcal{F}^{\mathscr{L}}(\mathbf{q}) + \mathbf{G}(\mathbf{q}) \tag{2.7}$$

with

$$\mathcal{F}^{\mathscr{L}}(\mathbf{q}) = \left\{ \begin{array}{c} \mathbf{V} \\ \frac{R}{c_v}\left(E - \rho g z\right)\mathcal{I} \\ \overline{h}\mathbf{V} \end{array} \right\}$$

and $\overline{h} = \frac{1}{\overline{\rho}}\left(\overline{E} + \overline{p}\right)$. The linearized form (2.7) represents the basis for the definition of the linear problem which will be discussed in section 4.4.

3. Temporal discretization. In this section we discuss the semi-implicit method adopted for the time discretization of system (2.5). We notice that, although the SI approach is usually considered in combination with either the Crank–Nicolson or the leapfrog time integration schemes, following the abstract formulation of [33] it is possible to include other time-integration schemes, such as the backward difference scheme presented in [35] and summarized in the sequel. We also notice that all these schemes can be modified to account for variable time-steps; however, we consider here for simplicity, the constant time-step case and leave the adaptive case, with the associated, nontrivial, issue of defining a criterion for varying the time increment, for a future work. We, thus, consider the abstract problem

$$\frac{d\mathbf{q}}{dt} = \widetilde{\mathscr{S}}(\mathbf{q}), \tag{3.1}$$

to be solved in $(0, T_{fin}]$ with a suitable initial condition, define an affine operator $\widetilde{\mathscr{A}}$ such that $\widetilde{\mathscr{A}}\mathbf{q} \approx \widetilde{\mathscr{S}}(\mathbf{q})$ and set

$$\frac{d\mathbf{q}}{dt} = \left\{\widetilde{\mathscr{S}}(\mathbf{q}) - \widetilde{\mathscr{A}}\mathbf{q}\right\} + \widetilde{\mathscr{A}}\mathbf{q}. \tag{3.2}$$

The main idea is now to treat the term in braces explicitly, while the remaining term will be treated implicitly. Notice that problem (2.5) can be recast in the form (3.1) by

TABLE 3.1
The θ-method (TM), leapfrog (LF2), and backward difference of order 2 (BDF2) and 3 (BDF3) time-integration schemes with their associated coefficients in the context of (3.4).

Method	α_0	α_1	α_2	γ	β_0	β_1	β_2	σ_{-1}	σ_0	σ_1	σ_2
TM	1	0	0	1	1	0	0	θ	$1-\theta$	0	0
LF2	0	1	0	2	1	0	0	θ	0	$1-\theta$	0
BDF2	$\frac{4}{3}$	$-\frac{1}{3}$	0	$\frac{2}{3}$	2	-1	0	1	0	0	0
BDF3	$\frac{18}{11}$	$-\frac{9}{11}$	$\frac{2}{11}$	$\frac{6}{11}$	3	-3	1	1	0	0	0

setting $\widetilde{\mathscr{S}}(\mathbf{q}) = \mathscr{S}^{NS}(\mathbf{q}) - T^{cv}(\mathbf{q}-\mathbf{q}_b)$. To allow for more flexibility in the treatment of the damping term, it is also convenient to further split the affine operator $\widetilde{\mathscr{A}}$ as $\widetilde{\mathscr{A}} = \mathscr{A} + \mathscr{A}^0$, and set $\mathscr{A}\mathbf{q} = \mathscr{L}\mathbf{q} + \mathbf{f}$ and $\mathscr{A}^0\mathbf{q} = \mathscr{L}^0\mathbf{q} + \mathbf{f}^0$, where $\mathbf{f}$ and $\mathbf{f}^0$ are assumed to be constant in time. Equation (3.2) can now be written as

$$\frac{d\mathbf{q}}{dt} = \{\mathscr{S}(\mathbf{q}) - \mathscr{L}\mathbf{q}\} + \mathscr{L}\mathbf{q} + \mathscr{L}^0\mathbf{q} + \mathbf{f}^0, \tag{3.3}$$

where $\mathscr{S}(\mathbf{q}) = \widetilde{\mathscr{S}}(\mathbf{q}) - \mathscr{A}^0\mathbf{q}$. Clearly, for a specific operator $\widetilde{\mathscr{S}}$ in (3.1), a proper definition of the linear and nonlinear operators in (3.3) is a critical step in the design of the numerical scheme. For the case of the Navier–Stokes system, this will be discussed in detail in section 5. For the present section, however, it is sufficient to consider the abstract form (3.3). Choosing now a time-step Δt, letting $t^n = n\Delta t$, with $n = 0, \ldots, T_{fin}/\Delta t$, and denoting by $\mathbf{q}^n$ the approximate solution at time level t^n, the discretization of (3.3) is constructed as follows:

$$\begin{aligned}
\frac{d\mathbf{q}}{dt} &\approx \frac{1}{\gamma\Delta t}\left[\mathbf{q}^{n+1} - \sum_{m=0}^{2}\alpha_m\mathbf{q}^{n-m}\right] \\
\{\mathscr{S}(\mathbf{q}) - \mathscr{L}\mathbf{q}\} &\approx \sum_{m=0}^{2}\beta_m\left(\mathscr{S}(\mathbf{q}^{n-m}) - \mathscr{L}\mathbf{q}^{n-m}\right) \\
\mathscr{L}\mathbf{q} &\approx \sum_{m=-1}^{2}\sigma_m\mathscr{L}\mathbf{q}^{n-m} \\
\mathscr{L}^0\mathbf{q} &\approx \mathscr{L}^0\mathbf{q}^{n+1}
\end{aligned} \tag{3.4}$$

for suitable coefficients γ, α_m, β_m, and σ_m. Notice that, for consistency, it is required that $\sum_m \alpha_m = \sum_m \beta_m = \sum_m \sigma_m = 1$. Typically, the operator $\mathscr{L}$ is chosen in such a way that, for a particular range of $\mathbf{q}$, the term $\mathscr{S} - \mathscr{L}$ vanishes, and time integration is performed with the implicit scheme $(3.4)_{1,3,4}$. In Table 3.1 it is shown how to recover some classical time-marching schemes by properly choosing the coefficients in (3.4), namely, the θ-method, the leap-frog method, the backward difference scheme (BDF) proposed in [35], and a third-order BDF scheme. Concerning accuracy, we have first order for the θ-method, second order for the leapfrog and BDF2 schemes, and third order for BDF3. Concerning stability, the amplification factors for the model equation

$$\frac{dq}{dt} = i\omega q,$$

where $i = \sqrt{-1}$ and $\omega \in \mathbb{R}$, are plotted in Figure 3.1 for both the explicit version (left) and the implicit version (right) of the considered time integrators. The methods which guarantee unconditional stability are the implicit TM, LF2, and BDF2. More details can be found in [33]. Having completely defined our time-integration

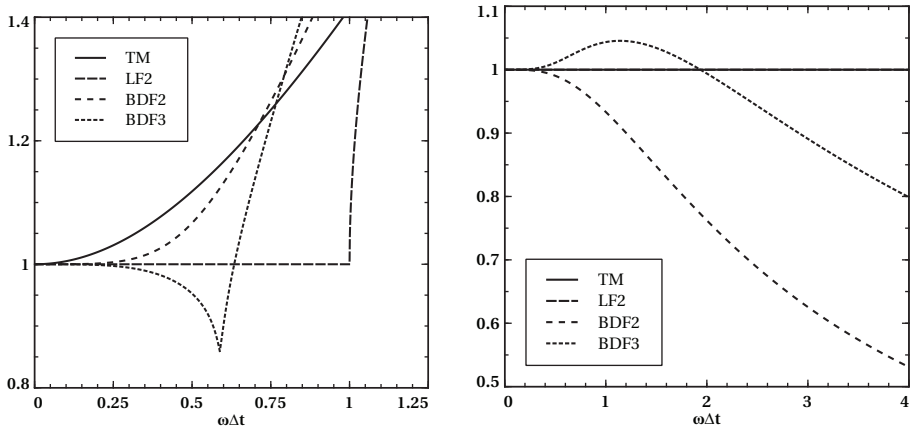

FIG. 3.1. *Amplification factors for the time integration schemes listed in Table* 3.1 *for the explicit (left) and the implicit (right) versions. For the TM and LF*2 *methods the choice* $\theta = 0.5$ *has been considered.*

method, it is important to notice that, in most numerical weather prediction codes, the semi-implicit method is usually implemented as an implicit correction to an explicit predictor substep [43]. In our case, this leads to the following algorithm:

(i) compute the explicit predictor step

$$\tilde{\mathbf{q}}^{ex} = \sum_{m=0}^{2} \alpha_m \mathbf{q}^{n-m} + \gamma \Delta t \sum_{m=0}^{2} \beta_m \mathscr{S}(\mathbf{q}^{n-m});$$

(ii) let $\rho_m = \sigma_m - \beta_m$, with $\beta_{-1} = 0$ and compute $\mathbf{q}^* = \rho_{-1}\tilde{\mathbf{q}}^{ex} + \sum_{m=0}^{2} \rho_m \mathbf{q}^{n-m}$;

(iii) let $\mathscr{B} = \left(\mathscr{I} - \gamma \Delta t \mathscr{L}^0\right)^{-1}$, where $\mathscr{I}$ is the identity, and compute the implicit corrector step

$$\left(\mathscr{I} - \rho_{-1}\left(\gamma \Delta t \mathscr{B}\mathscr{L}\right)\right)\mathbf{q}_{tt} = \mathscr{B}\mathbf{q}^* - \left(\gamma \Delta t \mathscr{B}\mathscr{L}^0\right)\left(\sum_{m=0}^{2} \rho_m \mathbf{q}^{n-m}\right) + \rho_{-1}\left(\gamma \Delta t \mathscr{B}\mathbf{f}^0\right);$$

notice that $\mathbf{q}_{tt}$ is an approximation of $\frac{d^2\mathbf{q}}{dt^2}$ (see [33]);

(iv) update the solution by setting $\mathbf{q}^{n+1} = \frac{1}{\rho_{-1}}(\mathbf{q}_{tt} - \sum_{m=0}^{2} \rho_m \mathbf{q}^{n-m})$.

4. Spatial discretization. In this section, we address the spatial discretization of (2.5) by resorting to a high-order, nodal, DG formulation. The general framework for such discretization is provided by [6, 5], while we refer to [30, 34, 32] for the aspects specifically related to the high-order approximation.

4.1. Notation. Let Ω be an open bounded domain of $\mathbb{R}^2$, with boundary $\partial\Omega$ and outward unit normal vector $\mathbf{n}_{\partial\Omega}$, and let $\mathscr{T}_h$ denote a partition of Ω into $\mathcal{N}_{el}$ nonoverlapping curvilinear quadrilateral elements K which are images of the reference element $\widehat{K} = [-1, 1]^2$ under smooth, bijective maps $\mathscr{F}_K$

$$\forall K \in \mathscr{T}_h : \quad K = \mathscr{F}_K\left(\widehat{K}\right).$$

The diameter of K is h_K and we let $h = \max_{K \in \mathscr{T}_h} h_K$. The set of the edges e of the triangulation is denoted by $\mathscr{E}_h$. Let ∂K and $\mathbf{n}_{e,\partial K}$ denote the boundary of $K \in \mathscr{T}_h$ and

the outward unit normal vector on each edge $e \in \partial K$, respectively, and $\partial\widehat{K}$ and $\mathbf{n}_{\hat{e},\partial\widehat{K}}$ denote the boundary and the outward unit normal vector for the reference element $\widehat{K}$. The notation $\mathbf{x} = \mathscr{F}_K(\boldsymbol{\xi})$, with $\mathbf{x} = (x, z) \in \Omega$, $\boldsymbol{\xi} = (\xi, \zeta) \in \widehat{K}$ will be used. We also associate with each local map the Jacobian $J_K = \frac{d\mathscr{F}_K}{d\boldsymbol{\xi}}$ and the determinant $|J_K|$. Although not essential, we will assume that $\mathscr{T}_h$ is conforming, that is, given K_1, $K_2 \in \mathscr{T}_h$ we either have that $K_1 \cap K_2$ is empty, or it is a vertex or a complete edge $e \in \mathscr{E}_h$. Following the usual notation in the context of DG formulation, we now define averages and jumps (see [16, 3]). Letting, thus, χ_h denote a generic function piecewise continuous on $\mathscr{T}_h$, for a given element K, edge $e \subset \partial K$ and point $\mathbf{x} \in e$ we define

$$\chi_h(\mathbf{x}^{int(K)}) = \lim_{\substack{\mathbf{y} \to \mathbf{x} \\ \mathbf{y} \in \mathring{K}}} \chi_h(\mathbf{y}), \qquad \chi_h(\mathbf{x}^{ext(K)}) = \lim_{\substack{\mathbf{y} \to \mathbf{x} \\ \mathbf{y} \notin K}} \chi_h(\mathbf{y}).$$

This definition can be extended to vector-valued functions by applying it componentwise. For $e = \partial K \cap \partial K'$, $\mathbf{x} \in e$, the average and jump for a scalar function χ_h and vector function $\mathbf{r}_h$ piecewise continuous on $\mathscr{T}_h$ are defined, respectively, as follows:

$$\begin{aligned}
\{\chi_h\}(\mathbf{x}) &= \frac{1}{2}(\chi_h(\mathbf{x}^{int(K)}) + \chi_h(\mathbf{x}^{int(K')})) \\
\{\mathbf{r}_h\}(\mathbf{x}) &= \frac{1}{2}(\mathbf{r}_h(\mathbf{x}^{int(K)}) + \mathbf{r}_h(\mathbf{x}^{int(K')})) \\
[\![\chi_h]\!](\mathbf{x}) &= \chi_h(\mathbf{x}^{int(K)})\mathbf{n}_{e,\partial K} + \chi_h(\mathbf{x}^{int(K')})\mathbf{n}_{e,\partial K'} \\
[\![[\![\mathbf{r}_h]\!]]\!](\mathbf{x}) &= \mathbf{r}_h(\mathbf{x}^{int(K)}) \otimes \mathbf{n}_{e,\partial K} + \mathbf{r}_h(\mathbf{x}^{int(K')}) \otimes \mathbf{n}_{e,\partial K'}.
\end{aligned} \tag{4.1}$$

Notice that $(4.1)_4$ differs from the usual definition of the jump for a vector-valued function, and this latter can be recovered as $[\![\mathbf{r}_h]\!] = \mathrm{Tr}\,([\![[\![\mathbf{r}_h]\!]]\!])$. Finally, we let $\max\{\chi_h(\mathbf{x})\} = \max\{\chi_h(\mathbf{x}^{int(K)}), \chi_h(\mathbf{x}^{int(K')})\}$.

4.2. High-order polynomial space. The logically square structure of the reference element $\widehat{K}$ significantly simplifies the construction of high-order polynomial bases, since the multidimensional basis can be obtained as a tensor-product of the one-dimensional basis. For an integer $k \geqslant 1$, letting $\mathbb{P}_k([a, b])$ denote the space of polynomial functions of degree less than or equal to k on $[a, b]$, we introduce the following two bases for $\mathbb{P}_k([-1, 1])$: $\{\varphi_i(\xi)\}_{i=0}^k$ is the Lagrangian (i.e., nodal) basis associated with an arbitrary set of nodes $\xi_i \in [-1, 1]$, while $\{\psi_i(\xi)\}_{i=0}^k$ is the Legendre (i.e., modal) basis (see [11]). We also define

$$\widehat{\Phi}_{ij}(\boldsymbol{\xi}) = \varphi_i(\xi)\varphi_j(\zeta) \quad \text{and} \quad \Phi_{K,ij}(\mathbf{x}) = \begin{cases} \left(\widehat{\Phi}_{ij} \circ \mathscr{F}_K^{-1}\right)(\mathbf{x}), & \mathbf{x} \in K \\ 0, & \mathbf{x} \notin K \end{cases}.$$

For simplicity, a cumulative index I, ranging from 1 to $\mathcal{N} = (k+1)^2\mathcal{N}_{el}$, is also biunivocally associated with the indexes (K, ij). Although, in principle, several choices for the nodes ξ_i are possible, a convenient one is represented by the Legendre–Gauss–Lobatto (LGL) points, defined as the roots of the polynomial $(1 - \xi^2)\psi_k'(\xi)$. As a matter of fact, these points are endowed with a Gaussian quadrature rule that can be exploited to improve the efficiency of the resulting scheme (see [11]). The finite element space is now defined as $V_h = span\{\Phi_I\}$, $I = 1, \ldots, \mathcal{N}$. Notice that functions in V_h are in general discontinuous across edges $e \in \mathscr{E}_h$.

As it will be clear from the forthcoming sections, the DG formulation requires the evaluation of both two-dimensional and one-dimensional integrals on K and ∂K, respectively. To this end, following [30] the following approximate quadrature rules will be adopted

$$\int_K \chi(\mathbf{x})\,\mathrm{d}\mathbf{x} = \int_{\widehat{K}} \chi(\mathbf{x}(\boldsymbol{\xi}))|J_K(\boldsymbol{\xi})|\,\mathrm{d}\boldsymbol{\xi} \approx \sum_{i,j=0}^{k} \chi(\mathbf{x}(\xi_i,\zeta_j))|J_K(\xi_i,\zeta_j)|\widehat{w}_i\widehat{w}_j \tag{4.2}$$

and

$$\begin{aligned}
\int_{\partial K} \chi(\sigma)\,\mathrm{d}\sigma &= \sum_{\widehat{e}\in\partial\widehat{K}} \int_{\widehat{e}} \chi(\mathbf{x}(\widehat{\sigma}))\,|J_K(\widehat{\sigma})|\,\left\|J_K^{-T}(\widehat{\sigma})\,\mathbf{n}_{\widehat{e},\partial\widehat{K}}\right\|_2 \mathrm{d}\widehat{\sigma} \\
&\approx \sum_{i=0}^{k} \chi(\mathbf{x}(\xi_i,\zeta_0))\,|J_K(\xi_i,\zeta_0)|\,\left\|J_K^{-T}(\xi_i,\zeta_0)\mathbf{n}_{\widehat{e}_1,\partial\widehat{K}}\right\|_2 \widehat{w}_i \\
&\quad + \sum_{j=0}^{k} \chi(\mathbf{x}(\xi_k,\zeta_j))\,|J_K(\xi_k,\zeta_j)|\,\left\|J_K^{-T}(\xi_k,\zeta_j)\mathbf{n}_{\widehat{e}_2,\partial\widehat{K}}\right\|_2 \widehat{w}_j \\
&\quad + \sum_{i=0}^{k} \chi(\mathbf{x}(\xi_i,\zeta_k))\,|J_K(\xi_i,\zeta_k)|\,\left\|J_K^{-T}(\xi_i,\zeta_k)\mathbf{n}_{\widehat{e}_3,\partial\widehat{K}}\right\|_2 \widehat{w}_i \\
&\quad + \sum_{j=0}^{k} \chi(\mathbf{x}(\xi_0,\zeta_j))\,|J_K(\xi_0,\zeta_j)|\,\left\|J_K^{-T}(\xi_0,\zeta_j)\mathbf{n}_{\widehat{e}_4,\partial\widehat{K}}\right\|_2 \widehat{w}_j,
\end{aligned} \tag{4.3}$$

where χ is a generic function piecewise continuous on $\mathscr{T}_h$, $\|\cdot\|_2$ is the Euclidean norm of a vector, ξ_i and ζ_i are Legendre–Gauss–Lobatto points previously introduced, and $\widehat{w}_i$ are the associated weights, defined as

$$\widehat{w}_i = \frac{2}{k(k+1)}\left(\frac{1}{\psi_k(\xi_i)}\right).$$

In the following, for $i,j = 0,\ldots,k$, we will let

$$w_{K,ij} = |J_K(\xi_i,\zeta_j)|\widehat{w}_i\widehat{w}_j,$$

$$\omega^e_{K,ij} = \begin{cases} |J_K(\xi_i,\zeta_j)|\,\left\|J_K^{-T}(\xi_i,\zeta_j)\mathbf{n}_{\widehat{e},\partial\widehat{K}}\right\|_2 \widehat{w}_i, & (j,\widehat{e}) \in \{(0,\widehat{e}_1),(k,\widehat{e}_3)\} \\ |J_K(\xi_i,\zeta_j)|\,\left\|J_K^{-T}(\xi_i,\zeta_j)\mathbf{n}_{\widehat{e},\partial\widehat{K}}\right\|_2 \widehat{w}_j, & (i,\widehat{e}) \in \{(0,\widehat{e}_2),(k,\widehat{e}_4)\} \\ 0 & \text{otherwise.} \end{cases}$$

Notice that the degree of exactness of the quadrature rules (4.2) and (4.3) is $2k-1$. Nonetheless, as discussed in [30], this approximation does not spoil the order of accuracy of the resulting DG formulation.

4.3. Discontinuous Galerkin discretization. We first rewrite (2.5) introducing the auxiliary variable $\mathcal{S}$ as:

$$\begin{cases} \dfrac{\partial \mathbf{q}}{\partial t} = -\nabla\cdot\mathcal{F}^e(\mathbf{q}) + \nabla\cdot\mathcal{F}^v(\mathbf{q},\mathcal{S}) + \mathbf{G}(\mathbf{q}) - T^{cv}\,(\mathbf{q}-\mathbf{q}_b) \\ \mathcal{S} - \nabla\mathbf{q} = 0 \end{cases} \tag{4.4}$$

to be solved in $\Omega\times(0,T_{fin}]$ with suitable initial and boundary conditions. An approximation $(\mathbf{q}_h,\mathcal{S}_h) = (\mathbf{q}_h(\mathbf{x},t),\mathcal{S}_h(\mathbf{x},t))$ to the solution $(\mathbf{q}(\mathbf{x},t),\mathcal{S}(\mathbf{x},t))$ of (4.4) is sought, such that $(\mathbf{q}_h,\mathcal{S}_h) \in (V_h)^4\times(V_h)^8$ at each time level. In the following, for

the sake of clarity we will often omit the dependence of $\mathbf{q}_h$ and $\mathcal{S}_h$ on $(\mathbf{x}, t)$. Also, all products, differential operators, and average and jump operators are intended to be applied separately to each density, momentum, and energy component of their arguments. Multiplying the two equations (4.4) by test functions $\boldsymbol{\chi}_h \in (V_h)^4$ and $\mathcal{R}_h \in (V_h)^8$, respectively, integrating over $K \in \mathscr{T}_h$ and replacing the exact solution by its approximation, we have

$$\begin{cases} \dfrac{d}{dt}\displaystyle\int_K \mathbf{q}_h \boldsymbol{\chi}_h \,\mathrm{d}\mathbf{x} = -\int_K \nabla\cdot\left[\mathcal{F}^e(\mathbf{q}_h) - \mathcal{F}^v(\mathbf{q}_h, \mathcal{S}_h)\right]\boldsymbol{\chi}_h \,\mathrm{d}\mathbf{x} \\ \qquad\qquad\qquad + \displaystyle\int_K \left[\mathbf{G}(\mathbf{q}_h) - T^{cv}\left(\mathbf{q}_h - \mathbf{q}_b\right)\right]\boldsymbol{\chi}_h \,\mathrm{d}\mathbf{x}, \qquad \forall \boldsymbol{\chi}_h \in (V_h)^4 \\ \displaystyle\int_K \mathcal{S}_h \cdot \mathcal{R}_h \,\mathrm{d}\mathbf{x} - \int_K \nabla \mathbf{q}_h \cdot \mathcal{R}_h \,\mathrm{d}\mathbf{x} = 0, \qquad \forall \mathcal{R}_h \in (V_h)^8. \end{cases}$$

Then, formally integrating by parts and introducing the numerical fluxes $\widehat{\mathcal{F}}^e(\mathbf{q}_h)$, $\widehat{\mathbf{q}}(\mathbf{q}_h, \mathcal{S}_h)$, and $\widehat{\mathcal{S}}(\mathbf{q}_h, \mathcal{S}_h)$, we obtain the following discrete problem:
find $(\mathbf{q}_h(\cdot,t),\, \mathcal{S}_h(\cdot,t)) \in (V_h)^4 \times (V_h)^8$ such that for all $t \in (0,\, T_{fin}]$ and $\forall K \in \mathscr{T}_h$:

(4.5)
$$\begin{cases} \dfrac{d}{dt}\displaystyle\int_K \mathbf{q}_h \boldsymbol{\chi}_h \,\mathrm{d}\mathbf{x} = \int_K \left[\mathcal{F}^e(\mathbf{q}_h) - \mathcal{F}^v(\mathbf{q}_h, \mathcal{S}_h)\right]\cdot\nabla\boldsymbol{\chi}_h \,\mathrm{d}\mathbf{x} \\ \qquad\qquad\qquad - \displaystyle\int_{\partial K}\left[\widehat{\mathcal{F}}^e(\mathbf{q}_h) - \mathcal{F}^v(\widehat{\mathbf{q}}, \widehat{\mathcal{S}})\right]\cdot \mathbf{n}_{\partial K}\boldsymbol{\chi}_h \,\mathrm{d}\sigma \\ \qquad\qquad\qquad + \displaystyle\int_K \left[\mathbf{G}(\mathbf{q}_h) - T^{cv}\left(\mathbf{q}_h - \mathbf{q}_b\right)\right]\boldsymbol{\chi}_h \,\mathrm{d}\mathbf{x}, \qquad \forall \boldsymbol{\chi}_h \in (V_h)^4 \\ \displaystyle\int_K \mathcal{S}_h \cdot \mathcal{R}_h \,\mathrm{d}\mathbf{x} + \int_K \mathbf{q}_h\, \nabla\cdot \mathcal{R}_h \,\mathrm{d}\mathbf{x} - \int_{\partial K} \widehat{\mathbf{q}}\mathbf{n}_{\partial K}\cdot \mathcal{R}_h \,\mathrm{d}\sigma = 0, \qquad \forall \mathcal{R}_h \in (V_h)^8. \end{cases}$$

Specification of the numerical fluxes completes now the definition of the scheme. Concerning the hyperbolic flux, we consider here the Rusanov flux (see [45, 54])

$$\widehat{\mathcal{F}}^e(\mathbf{q}_h) = \{\mathcal{F}^e(\mathbf{q}_h)\} + \frac{|\lambda|}{2}[\![\mathbf{q}_h]\!], \tag{4.6}$$

where $|\lambda| = \max\{|\mathbf{v}_h \cdot \mathbf{n}| + a_h\}$, $\mathbf{v}_h$ and a_h denoting the wind velocity and sound speed associated with $\mathbf{q}_h$, respectively. The sound speed is in turn defined as $a = \sqrt{\gamma RT}$, with $\gamma = c_p/c_v$. We notice that more sophisticated choices than (4.6) are also possible, such as the HLL, HLLC, or Roe's fluxes (see [54] and also [19] for comments about the effect of the numerical flux on the computed solution). Concerning the viscous terms, the Bassi and Rebay method of [5], which is a particular case of the local discontinuous Galerkin approach described in [17], is adopted. We, thus, set

$$\widehat{\mathbf{q}} = \{\mathbf{q}_h\}, \qquad \widehat{\mathcal{S}} = \{\mathcal{S}_h\}. \tag{4.7}$$

Remark 4.1. When T^{cv} vanishes, i.e., far from the open boundaries, the conservation properties of (4.5) follow naturally from its flux-form, which can be made explicit by taking the test function $\boldsymbol{\chi}_h$ equal to the characteristic function of $K \in \mathscr{T}_h$, yielding

$$\frac{d}{dt}\int_K \mathbf{q}_h \,\mathrm{d}\mathbf{x} = -\int_{\partial K}\left[\widehat{\mathcal{F}}^e(\mathbf{q}_h) - \mathcal{F}^v(\widehat{\mathbf{q}}, \widehat{\mathcal{S}})\right]\cdot \mathbf{n}_{\partial K} \,\mathrm{d}\sigma + \int_K \mathbf{G}(\mathbf{q}_h)\,\mathrm{d}\mathbf{x},$$

and by noting that the numerical fluxes are single valued on $\mathscr{E}_h$. Notice also that discrete conservation is guaranteed regardless of the approximate evaluation of the area and boundary integrals.

We now take the test function $\boldsymbol{\chi}_h$ in $(4.5)_1$ equal to Φ_I. The left-hand side can be written as

$$\frac{d}{dt}\int_K \mathbf{q}_h \Phi_I \,\mathrm{d}\mathbf{x} = M\frac{d\mathbf{q}_h}{dt}, \tag{4.8}$$

with

$$M_{IJ} = \int_K \Phi_I \Phi_J \,\mathrm{d}\mathbf{x} = w_I \delta_{IJ}. \tag{4.9}$$

The right-hand side defines the operator

$$\begin{aligned}\left(\mathscr{S}_h^{NS}(\mathbf{q}_h)\right)_I = &\int_K \left[\mathcal{F}^e(\mathbf{q}_h) - \mathcal{F}^v(\mathbf{q}_h, \mathcal{S}_h)\right]\cdot\nabla\Phi_I \,\mathrm{d}\mathbf{x}\\ &- \int_{\partial K}\left[\widehat{\mathcal{F}}^e(\mathbf{q}_h) - \mathcal{F}^v(\hat{\mathbf{q}}, \hat{\mathcal{S}})\right]\cdot\mathbf{n}_{\partial K}\Phi_I \,\mathrm{d}\sigma + \int_K \mathbf{G}(\mathbf{q}_h)\Phi_I \,\mathrm{d}\mathbf{x}\end{aligned} \tag{4.10}$$

for $I = 1,\ldots,\mathcal{N}$; $\mathscr{S}_h^{NS}$ is the discrete counterpart of $\mathscr{S}^{NS}$ in (2.5). Finally, the remaining terms, associated with the damping layer, will be considered in section 4.4.

4.4. The linear problem. Proceeding as done in section 2.2 to define $\mathscr{L}^{NS}$ in (2.7) from $\mathscr{S}^{NS}$ in (2.5), we identify within (4.10) the following linear operator

$$\left(\mathscr{L}_h^{NS}\mathbf{q}_h\right)_I = \int_K \mathcal{F}^{\mathscr{L}}(\mathbf{q}_h)\cdot\nabla\Phi_I \,\mathrm{d}\mathbf{x} - \int_{\partial K}\widehat{\mathcal{F}}^{\mathscr{L}}(\mathbf{q}_h)\cdot\mathbf{n}_{\partial K}\Phi_I \,\mathrm{d}\sigma + \int_K \mathbf{G}(\mathbf{q}_h)\Phi_I \,\mathrm{d}\mathbf{x}, \tag{4.11}$$

for $I = 1,\ldots,\mathcal{N}$. In (4.11) the linear numerical flux is

$$\widehat{\mathcal{F}}^{\mathscr{L}} = \left\{\mathcal{F}^{\mathscr{L}}\right\} + \frac{|\overline{\lambda}|}{2}[\![\mathbf{q}_h]\!],$$

where $|\overline{\lambda}| = \overline{a} = \sqrt{\gamma R\overline{T}}$ and $\overline{T}$ is the temperature of the reference state, which is assumed to be a continuous function over $\overline{\Omega}$. We notice that the linear operator $\mathscr{L}_h^{NS}$ represents the approximate counterpart, using the DG finite element method supplied with the Rusanov numerical flux, of the corresponding space-continuous operator $\mathscr{L}^{NS}$ introduced in (2.7). In other words, $\mathscr{L}_h^{NS}$ represents in itself a consistent DG discretization of the linearized Euler equations. In addition, in order to deal with the damping terms in $(4.5)_1$, we define

$$\left(\mathscr{L}_h^0\mathbf{q}_h\right)_I = -\int_K T^{cv}\mathbf{q}_h\Phi_I \,\mathrm{d}\mathbf{x}, \qquad \mathbf{f}_I^0 = \int_K T^{cv}\mathbf{q}_b\Phi_I \,\mathrm{d}\mathbf{x}, \tag{4.12}$$

for $I = 1,\ldots,\mathcal{N}$.

5. The fully discrete problem. The fully discrete space-time approximation of problem (2.5) is obtained by properly substituting into the multistep time-advancing algorithm illustrated in section 3 the time derivative (4.8) and the discrete operators $\mathscr{S}_h^{NS}(\mathbf{q}_h)$, $\mathscr{L}_h^{NS}\mathbf{q}_h$, $\mathscr{L}_h^0\mathbf{q}_h$ and $\mathbf{f}^0$ introduced in (4.10), (4.11), and (4.12), respectively. At each time level, $\mathcal{S}_h$ is computed from $(4.5)_2$.

5.1. Filtering the high-frequency modes. The DG method using high-order basis functions can be regarded as a spectral element method with no continuity constraint among neighboring elements. Since high-order methods do not present any intrinsic numerical diffusion, they are prone to instabilities due to nonlinear mixing

and the Gibbs phenomenon, particularly in the case of poorly resolved flows (see [9]). The usual way of dealing with this instability in the context of spectral formulations is to introduce a filtering operator which damps the high frequency modes without altering the low frequency modes. This is done by transforming from nodal representation to modal representation, applying a lowpass filter, and then by transforming back to nodal representation. In the present paper, filtering is performed using a similar strategy as in [30], and the action of the filter is included in $\mathscr{S}_h^{NS}$. It should be mentioned that the DG need for a filter arises only due to our particular choice of inexact integration rules (of order $2k-1$); choosing $2k$ integration rules obviates the need for a filter, but the cost of the method increases due to the need to invert a nondiagonal (albeit small) mass matrix. Furthermore, having a nondiagonal mass matrix complicates the construction of the pseudo-Helmholtz problem; this, in fact, is the key to the success of the semi-implicit time-integration method.

5.2. Solution algorithm for the pseudo-Helmholtz operator problem. The linear system arising from the SI time discretization is usually dealt with by properly combining the continuity, momentum, and energy equations, in such a way to obtain an algebraically equivalent problem of diffusion-reaction type, referred to as the pseudo-Helmholtz operator problem, for the sole pressure variable. This equivalent reformulation has the computational advantage of reducing considerably the dimension of the problem; moreover, if an iterative solver is adopted, it produces a significant acceleration of the convergence rate and simplifies the definition of the stopping criterion. Based on these considerations, an extension of the above approach to the present semi-implicit DG setting is highly desirable, albeit being far from trivial. Nevertheless, such an extension can be made possible by conveniently exploiting the structure of the approximate quadrature rules (4.2) and (4.3). By doing so, one obtains a formulation that can be regarded as a LDG discretization of a diffusion-reaction problem for the pressure variable where the auxiliary flux unknown is statically condensed out by proper use of mass lumping. In this sense, the resulting discrete scheme shares some similarities with hybridized dual mixed methods where static condensation is the crucial approach to obtaining a linear algebraic problem for the sole primal variable (see [4] for an introduction to static condensation at the discrete level, and [15, 14] for a more recent development on this subject). In the following, the two terms static condensation and pseudo-Helmholtz form will be used interchangeably.

For simplicity, we assume here that periodic boundary conditions are prescribed and we do not include the gravity terms into the implicit part of the problem. We set $\mathbf{V} = [U, W]^T$ and denote by $\widehat{\mathbf{F}}_\rho^{\mathscr{L}}$, $\widehat{\mathcal{F}}_{\mathbf{V}}^{\mathscr{L}}$, and $\widehat{\mathbf{F}}_E^{\mathscr{L}}$ the rows in $\widehat{\mathcal{F}}^{\mathscr{L}}$ corresponding to density, momentum, and energy, respectively. Under these assumptions, the linear problem arising from the SI-DG formulation reads:
find $(\rho_{tt}, \mathbf{V}_{tt}, E_{tt}, p_{tt}) \in V_h \times (V_h)^2 \times V_h \times V_h$ such that $\forall K \in \mathscr{T}_h$, $I = 1, \dots, \mathcal{N}$:

(5.1)
$$\int_K \rho_{tt}\Phi_I \,\mathrm{d}\mathbf{x} - \alpha \int_K \mathbf{V}_{tt} \cdot \nabla\Phi_I \,\mathrm{d}\mathbf{x} + \alpha \int_{\partial K} \widehat{\mathbf{F}}_\rho^{\mathscr{L}} \cdot \mathbf{n}_{\partial K}\Phi_I \,\mathrm{d}\sigma = \int_K \rho^*\Phi_I \,\mathrm{d}\mathbf{x}$$
$$\int_K \mathbf{V}_{tt}\Phi_I \,\mathrm{d}\mathbf{x} - \alpha \int_K p_{tt}\mathcal{I} \cdot \nabla\Phi_I \,\mathrm{d}\mathbf{x} + \alpha \int_{\partial K} \widehat{\mathcal{F}}_{\mathbf{V}}^{\mathscr{L}} \cdot \mathbf{n}_{\partial K}\Phi_I \,\mathrm{d}\sigma = \int_K \mathbf{V}^*\Phi_I \,\mathrm{d}\mathbf{x}$$
$$\int_K E_{tt}\Phi_I \,\mathrm{d}\mathbf{x} - \alpha \int_K \overline{h}\mathbf{V}_{tt} \cdot \nabla\Phi_I \,\mathrm{d}\mathbf{x} + \alpha \int_{\partial K} \widehat{\mathbf{F}}_E^{\mathscr{L}} \cdot \mathbf{n}_{\partial K}\Phi_I \,\mathrm{d}\sigma = \int_K E^*\Phi_I \,\mathrm{d}\mathbf{x}$$
$$\int_K p_{tt}\Phi_I \,\mathrm{d}\mathbf{x} = \frac{R}{c_v} \int_K E_{tt}\Phi_I \,\mathrm{d}\mathbf{x}$$

with $\alpha = \rho_{-1}\gamma\Delta t$. Equations $(5.1)_{2,3,4}$ then immediately provide the problem: find $(p_{tt}, \mathbf{V}_{tt}) \in V_h \times (V_h)^2$ such that $\forall K \in \mathscr{T}_h$, $I = 1, \dots, \mathcal{N}$

(5.2)
$$\int_K p_{tt}\Phi_I \,\mathrm{d}\mathbf{x} - \alpha\frac{R}{c_v}\int_K \overline{h}\mathbf{V}_{tt}\cdot\nabla\Phi_I \,\mathrm{d}\mathbf{x} + \alpha\frac{R}{c_v}\int_{\partial K}\overline{h}\,\widehat{\mathbf{V}}\cdot\mathbf{n}_{\partial K}\Phi_I \,\mathrm{d}\sigma = \int_K p^*\Phi_I \,\mathrm{d}\mathbf{x}$$
$$\int_K \mathbf{V}_{tt}\cdot\boldsymbol{\Phi}_I \,\mathrm{d}\mathbf{x} - \alpha\int_K p_{tt}\nabla\cdot\boldsymbol{\Phi}_I \,\mathrm{d}\mathbf{x} + \alpha\int_{\partial K}(\widehat{p}\,\mathbf{n}_{\partial K})\cdot\boldsymbol{\Phi}_I \,\mathrm{d}\sigma = \int_K \mathbf{V}^*\cdot\boldsymbol{\Phi}_I \,\mathrm{d}\mathbf{x},$$

where $\boldsymbol{\Phi}_I = [\Phi_I, 0]^T$ or $\boldsymbol{\Phi}_I = [0, \Phi_I]^T$, $p^* = \frac{R}{c_v}E^*$, and the numerical fluxes are

$$\widehat{\mathbf{V}} = \{\mathbf{V}_{tt}\} + \frac{|\overline{\lambda}|}{2}\frac{c_v}{R\overline{h}_h}[\![p_{tt}]\!], \qquad \widehat{p} = \{p_{tt}\}\mathcal{I} + \frac{|\overline{\lambda}|}{2}[\![\![\mathbf{V}_{tt}]\!]\!]. \tag{5.3}$$

Problem (5.2) can be fully regarded as the LDG discretization of the following elliptic problem for the sole pressure variable (see equations (2.2) and (2.3) in [13])

$$-\alpha^2\nabla\cdot\left(\overline{a}^2\nabla p_{tt}\right) + p_{tt} = -\alpha\nabla\cdot\left(\overline{a}^2\mathbf{V}^*\right) + p^* \tag{5.4}$$

supplied with numerical fluxes (5.3), except for the fact that $[\![\![\mathbf{V}_{tt}]\!]\!]$ is used in $(5.3)_2$ instead of $[\![\mathbf{V}_{tt}]\!]$.

Remark 5.1. The elliptic numerical fluxes (5.3) descend from the hyperbolic numerical flux (4.6). In particular, the dissipative term $\frac{|\lambda|}{2}[\![\mathbf{q}_h]\!]$ in this latter flux gives rise to the two stabilization terms in (5.3).

As discussed in [13], the inclusion of the jump term in $(5.3)_2$ makes it impossible to compute $\mathbf{V}_{tt}$ *element by element* in terms of p_{tt} from $(5.2)_2$. This implies that, starting from (5.2), it is not possible to obtain in an efficient way a discrete counterpart of (5.4) involving the sole pressure variable. However, we show now how, by taking advantage of the approximate quadrature rule, it is possible to compute $\mathbf{V}_{tt}$ *node by node* in terms of p_{tt}. To this end, we need to work out the matrix formulation of (5.2), and some additional notation is required. We denote by $\mathcal{M}$ the number of quadrature nodes in $\mathscr{T}_h$, and assume without loss of generality that the first $\mathcal{M}^{\mathscr{E}}$ of such nodes are located on $\mathscr{E}_h$. For the Qth quadrature node, we denote by $I_q(Q)$ the degrees of freedom collocated at the quadrature node itself, with $q = 1, \dots, n_Q$. For $Q > \mathcal{M}^{\mathscr{E}}$ we have $n_Q = 1$; for $Q \leqslant \mathcal{M}^{\mathscr{E}}$, on the one hand, we have $n_Q \geqslant 2$ thanks to the periodic boundary conditions and, on the other hand, the regularity of $\mathscr{T}_h$ implies an upper bound for n_Q. Symmetrically, for a degree of freedom I we denote by $Q(I)$ the corresponding quadrature node. Notice that, for a continuous function χ, we have $\chi_{I_{q_1}(Q)} = \chi_{I_{q_2}(Q)} = \chi_Q$. For a given pair (Q, e), with Q collocated on e, we use the shorthand notation $I_{Q,e}$, $I'_{Q,e}$ to indicate two degrees of freedom such that $I_{Q,e} \neq I'_{Q,e}$, $Q(I_{Q,e}) = Q(I'_{Q,e})$, and $I_{Q,e}$ and $I'_{Q,e}$ belong to a couple of elements K, K' such that $\partial K \cap \partial K' = e$. Notice that the subscript (Q, e) will be usually omitted, since it is clear from the context. Finally, for $I = (K, ij)$ we denote by $\mathscr{E}_I$ the set of edges e such that $e \in \partial K$ and $Q(I)$ is collocated on e.

The integrals on the interior of K can be easily expressed in terms of the $\mathcal{N}\times\mathcal{N}$ matrices M, D_x, and D_z defined, respectively, in (4.9) and by

$$(D_x)_{IJ} = -\int_K \frac{\partial\Phi_I}{\partial x}\Phi_J \,\mathrm{d}\mathbf{x}, \quad (D_z)_{IJ} = -\int_K \frac{\partial\Phi_I}{\partial z}\Phi_J \,\mathrm{d}\mathbf{x}, \tag{5.5}$$

which, due to the discontinuous nature of the basis functions, are block-diagonal. Concerning the boundary integrals, we illustrate the treatment of $(5.2)_1$, as analogous

considerations apply to $(5.2)_2$. Dropping the subscript tt for simplicity, we have

$$\begin{aligned}
&\int_{\partial K} \frac{R}{c_v}\overline{h}\,\widehat{\mathbf{V}}\cdot\mathbf{n}_{\partial K}\Phi_I\,\mathrm{d}\sigma \\
&\quad= \sum_{e\in\mathscr{E}_I}\omega_I^e\left\{\frac{\left|\overline{\lambda}_I\right|}{2}\left(p_I-p_{I'}\right)+\frac{1}{2}\frac{R\overline{h}_I}{c_v}\left[\left(U_I+U_{I'}\right)n_x+\left(W_I+W_{I'}\right)n_z\right]\right\} \\
&\quad= \frac{\left|\overline{\lambda}_{Q(I)}\right|}{2}\sum_{e\in\mathscr{E}_I}\omega_I^e\left(p_I-p_{I'}\right)+\frac{1}{2}\frac{R\overline{h}_{Q(I)}}{c_v}\sum_{e\in\mathscr{E}_I}\omega_I^e\left[\left(U_I+U_{I'}\right)n_x+\left(W_I+W_{I'}\right)n_z\right].
\end{aligned}$$

Let now D^s, BN_x, and BN_z denote the $\mathcal{N}\times\mathcal{N}$ matrices such that

$$\left(D^s q_h\right)_I=\frac{1}{2}\sum_{e\in\mathscr{E}_I}\omega_I^e\left(q_I-q_{I'}\right),\qquad \left(BN_{x,z}q_h\right)_I=\frac{1}{2}\sum_{e\in\mathscr{E}_I}\omega_I^e\left(q_I+q_{I'}\right)n_{x,z}$$

with q_h denoting either p_h, U_h, or W_h. It is easy to verify that, up to a permutation of the unknowns, D^s, BN_x, and BN_z have a block-diagonal structure with $\mathcal{M}^{\mathscr{E}}$ nonzero blocks of dimension n_Q, $Q=1,\ldots,\mathcal{M}^{\mathscr{E}}$, respectively. In particular, for the case of a quadrature node belonging to one sole edge e (i.e., not corner point), we have $n_Q=2$ and the 2×2 blocks

$$D_Q^s=\frac{1}{2}\begin{bmatrix}1 & -1\\ -1 & 1\end{bmatrix}\omega_Q^e,$$

and

$$BN_{x_Q}=\frac{1}{2}\begin{bmatrix}n_{x_{e,I_1(Q)}} & n_{x_{e,I_1(Q)}}\\ n_{x_{e,I_2(Q)}} & n_{x_{e,I_2(Q)}}\end{bmatrix}\omega_Q^e,\qquad BN_{z_Q}=\frac{1}{2}\begin{bmatrix}n_{z_{e,I_1(Q)}} & n_{z_{e,I_1(Q)}}\\ n_{z_{e,I_2(Q)}} & n_{z_{e,I_2(Q)}}\end{bmatrix}\omega_Q^e,$$

with $\omega_Q^e=\omega_{I_{Q,e}}^e=\omega_{I'_{Q,e}}^e$.

Summarizing, the matrix counterpart of (5.2) after proper use of numerical integration reads

$$\begin{cases}\left(M+\alpha\Lambda D^s\right)p+\alpha\left[\left(D_x+BN_x\right)AU+\left(D_z+BN_z\right)AW\right]=Mp^*\\ \left(M+\alpha\Lambda D^s\right)U+\alpha\left(D_x+BN_x\right)p=MU^*\\ \left(M+\alpha\Lambda D^s\right)W+\alpha\left(D_z+BN_z\right)p=MW^*,\end{cases}\tag{5.6}$$

where Λ and A are $\mathcal{N}\times\mathcal{N}$ diagonal matrices defined as

$$\Lambda_{IJ}=\left|\overline{\lambda}_{Q(I)}\right|\delta_{IJ},\quad A_{IJ}=\frac{R}{c_v}\overline{h}_{Q(I)}\delta_{IJ}.$$

The key element for the reformulation of (5.6) in terms of the sole unknown p relies on an efficient computation of the inverse of the matrix $M^{DG}=M+\alpha\Lambda D^s$. We have

$$\left(M^{DG}\right)^{-1}=\left(I+\alpha\Lambda M^{-1}D^s\right)^{-1}M^{-1}:=\Sigma M^{-1}.$$

Since $\Sigma^{-1}=(I+\alpha\Lambda M^{-1}D^s)$, it turns out that Σ has the same block-diagonal structure as D^s, so that its computation is straightforward (see Figure 5.1).

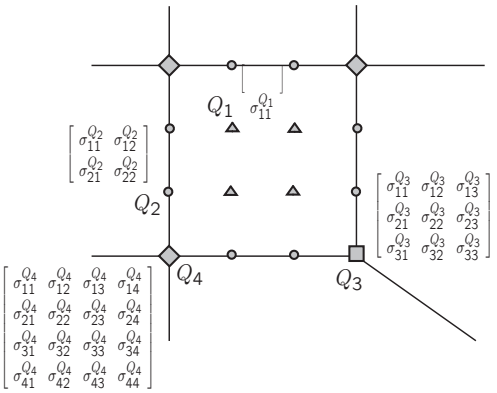

FIG. 5.1. *Representation of the block-diagonal structure of the matrix* Σ. *A* 1×1 *block is associated with internal quadrature nodes* ($\triangle$) *such as* Q_1, *and we have* $\sigma_{11}^{Q_1} = 1$. *Quadrature nodes belonging to one sole edge* ($\circ$), *such as* Q_2, *give rise to* 2×2 *blocks. Finally, nodes belonging to two or more edges* ($\square$ *and* $\diamond$), *such as* Q_3 *and* Q_4, *give rise to* $n_Q \times n_Q$ *blocks.*

Upon defining $\tilde{D}_x^{DG} = (M^{DG})^{-1}(D_x + BN_x)$, $\tilde{D}_z^{DG} = (M^{DG})^{-1}(D_z + BN_z)$, $\tilde{p} = \Sigma p^*$, $\tilde{U} = \Sigma U^*$, and $\widetilde{W} = \Sigma W^*$, system (5.6) can be written as

$$\begin{cases} p + \alpha \left[\tilde{D}_x^{DG} A\, U + \tilde{D}_z^{DG} A\, W \right] = \tilde{p} \\ U + \alpha \tilde{D}_x^{DG} p = \tilde{U} \\ W + \alpha \tilde{D}_z^{DG} p = \widetilde{W}. \end{cases} \tag{5.7}$$

Substituting $(5.7)_{2,3}$ into $(5.7)_1$ we obtain

$$p - \alpha^2 \left(\tilde{D}_x^{DG} A \tilde{D}_x^{DG} + \tilde{D}_z^{DG} A \tilde{D}_z^{DG} \right) p = \tilde{p} - \alpha \left(\tilde{D}_x^{DG} A\, \tilde{U} + \tilde{D}_z^{DG} A\, \widetilde{W} \right). \tag{5.8}$$

Problem (5.8) is the discrete counterpart of (5.4). The advantages of solving (5.8) instead of (5.6) will be numerically demonstrated in section 6.1.

6. Numerical results. In this section, the numerical validation of the proposed scheme is carried out. To simplify the presentation, rather than giving a detailed description of each test case setup, we provide references to some classical works in the literature. In addition, a comprehensive overview of all the test cases can be found in [31]. For ease of comparison with the literature, all the results are converted to primitive variables: π is the Exner pressure, u and w are the horizontal and vertical velocities, respectively, and θ is the potential temperature. Deviations from the background atmosphere, which is characterized by a uniform Brunt–Väisälä frequency $N = \frac{g}{\theta}\frac{d\theta}{dz}$ (see [25]), are displayed. Following [48], the reference state $\overline{\mathbf{q}}$ (see section 2) is isothermal in all the test cases, with $\overline{T}$ being the highest temperature in the initial condition. The local Courant number and advective Courant number are defined as $C = \frac{a\Delta t}{h_{LGL}}$ and $C_{adv} = \frac{v\Delta t}{h_{LGL}}$, respectively, where h_{LGL} denotes the (variable) spacing between the Legendre–Gauss–Lobatto points (see section 4.2), a is the sound speed, and v is the wind velocity. The maximum values of C and C_{adv} in the domain are denoted by $C^{\max}$ and $C_{adv}^{\max}$, respectively. All the computations described in this section employ the BDF2 scheme of Table 3.1; notice, however, that similar results are obtained with the TM and LF2 schemes. To compare our results with other results

in the literature, it is convenient, for a given grid of high-order elements, to define the equivalent resolution as the resolution of a uniform grid with the same number $\mathcal{M}$ of grid points. The static condensation procedure described in section 5.2 is tested for the case of periodic and no-flux boundary conditions and implicit treatment of the acoustic waves in section 6.1. For the remaining test cases, the linear system, which includes an implicit treatment of the gravity waves, is solved in its complete form; we plan to extend the static condensation procedure to the general case in future work. Finally, for the mountain waves test cases the root-mean-square (RMS) errors are computed as in [31].

6.1. Bubble convection experiments. In this section, we study four idealized test cases characterized by buoyancy driven flows. In these tests, a basic-state atmosphere is considered, which is assumed to be at rest and in hydrostatic equilibrium, and a thermal anomaly, with a consequent density perturbation, is introduced.

The first test case aims at verifying the advantages of the semi-implicit time discretization in the case where only periodic boundary conditions are prescribed. The computational domain is the rectangle $[0\,m, 1000\,m] \times [0\,m, 2000\,m]$, and the initial datum is represented by a thermal anomaly introduced in an isothermal atmosphere at $T = 303\,K$ (notice that, thanks to this choice, the deviations from the reference atmosphere are zero far from the thermal anomaly, which satisfies the periodic boundary conditions at the top and bottom boundaries). The thermal anomaly has amplitude $-15\,K$ and has the same smooth profile described in [44]. Viscosity is set equal to $0.2\,m^2/s$. The computational grid is composed of 25×50, 10^{th}-order elements, with equivalent resolution $4\,m$, while the time-step is $0.02\,s$, yielding $C^{\max} = 6.1$ and $C^{\max}_{adv} = 0.15$. The computed potential temperature is displayed in Figure 6.1. For this particular computation, a comparison between the solutions computed with and without performing the static condensation shows that the number of GMRES iterations required for the solution of the linear system decreases by approximately a factor 2, while a rough comparison with the explicit time integration indicates a reduction in the overall computational time of approximately a factor 5. To confirm this result, the same test case has been repeated with different values of $C^{\max}$, using a coarser mesh of 12×24, 10^{th}-order elements. In Figure 6.2 the number of GMRES iterations per time step, the total number of GMRES iterations, and total CPU time

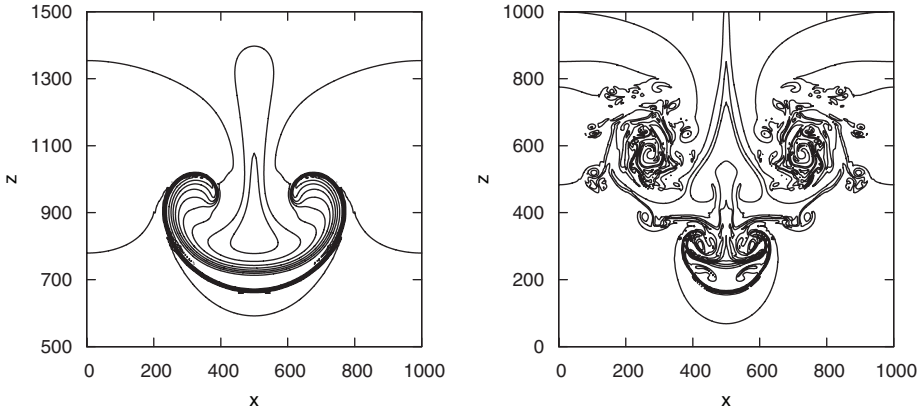

FIG. 6.1. *Cold bubble test case, potential temperature perturbation at time levels* $100\,s$ *(left) and* $200\,s$ *(right). Contour plots using values between* $-11.5\,K$ *and* $8\,K$ *with an interval of* $1.625\,K$.

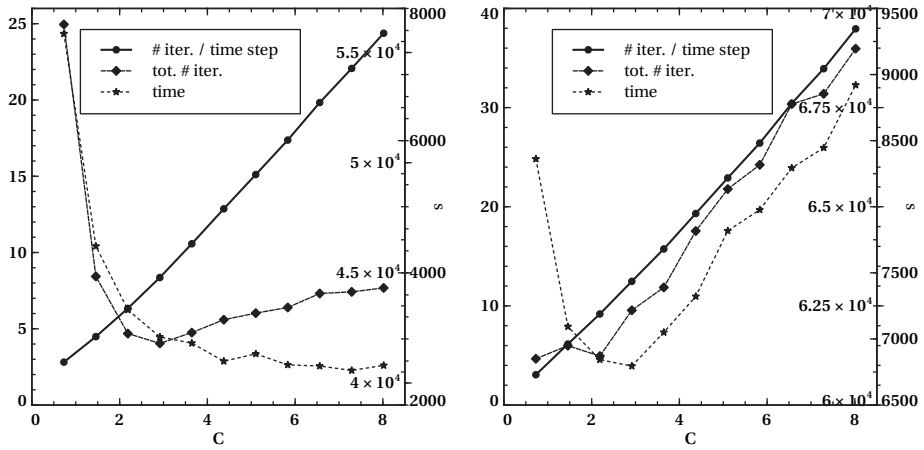

FIG. 6.2. *Cold bubble test case, number of GMRES iterations per time step (•, left axis), total number of GMRES iterations (♦, first right axis), and total CPU time (★, second right axis) as functions of* $C^{\max}$ *for the case of static condensation (left) and no static condensation (right).*

are plotted as functions of $C^{\max}$ for the case of static condensation (left) and no static condensation (right). The total time for the same computation using an explicit BDF method is $1.33 \cdot 10^4\, s$; using the largest Courant number possible we note in Figure 6.2 that the semi-implicit method with static condensation yields a CPU time of less than $2500\, s$, which is a factor of 5 smaller than the explicit result. From these results, it is clear that the semi-implicit time discretization increases the efficiency of the scheme for a wide range of Courant numbers, and that there is a substantial benefit in using the static condensation procedure. The improvement associated with the static condensation is due partly to a reduction in the number of GMRES iterations and partly to a minor cost of each iteration, since the unknown is represented by the sole pressure variable.

The second test case is similar to the smooth bubble test proposed in [12, 44]. The basic state atmosphere is characterized by neutral stratification, and the flow is driven by a smooth thermal anomaly of which the maximum amplitude is $+0.5\, K$. Reflecting boundary conditions are applied and the flow is inviscid. The computational domain is $[0\, m, 1000\, m] \times [0\, m, 1000\, m]$ and a grid composed of 20×20, 10^{th}-order elements is adopted, with equivalent resolution $5\, m$. The time-step is $0.08\, s$, yielding $C^{\max} = 19$ and $C^{\max}_{adv} = 0.12$. Figure 6.3 shows the computed potential temperature perturbation at $T_{fin} = 600\, s$ and the one-dimensional profile along $z = 700\, m$ for the same quantity. Minimum and maximum values for the computed solution are $(-1.125 \cdot 10^{-5}, 5.016 \cdot 10^{-6})$ for π, $(-2.161\, m/s, 2.161\, m/s)$ for u, $(-1.967\, m/s, 2.758\, m/s)$ for w, and $(-7.303 \cdot 10^{-2}\, K, 5.259 \cdot 10^{-1}\, K)$ for θ. All these results are in good agreement with those reported in [31] for the explicit case. Concerning conservation, for this problem we expect mass and total energy to remain constant. This is verified up to machine precision in the numerical simulation, where we observe for these quantities relative deviations equal to $8.755 \cdot 10^{-11}$ and $4.627 \cdot 10^{-11}$, respectively.

The third test case is analogous to the second one, except that a nonsmooth thermal anomaly is considered and the computational domain is larger. A very similar test case was also proposed in [44]. To deal with the nonsmooth initial datum, a viscosity $\nu = 0.4\, m^2/s$ is introduced, and we assume $Pr = 1$. Reflecting boundary

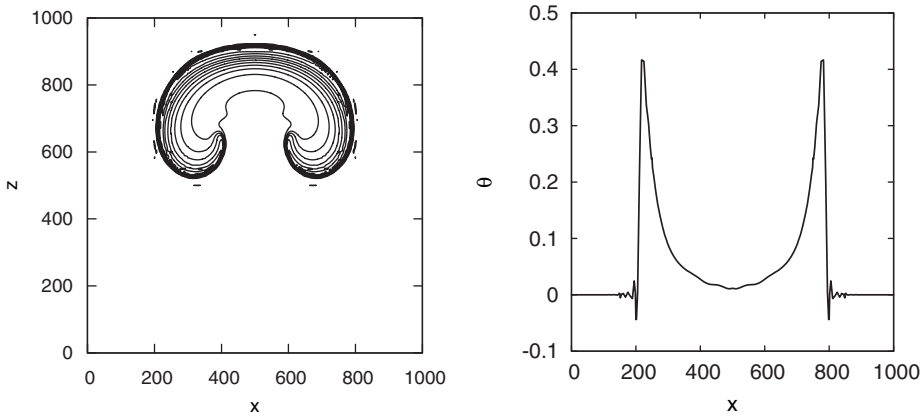

FIG. 6.3. *Smooth bubble test case, potential temperature perturbation at time level* $600\,s$. *Left: contour plot using values between* $0.025\,K$ *and* $0.525\,K$ *with an interval of* $0.05\,K$. *Right: profile along constant height* $z = 700\,m$.

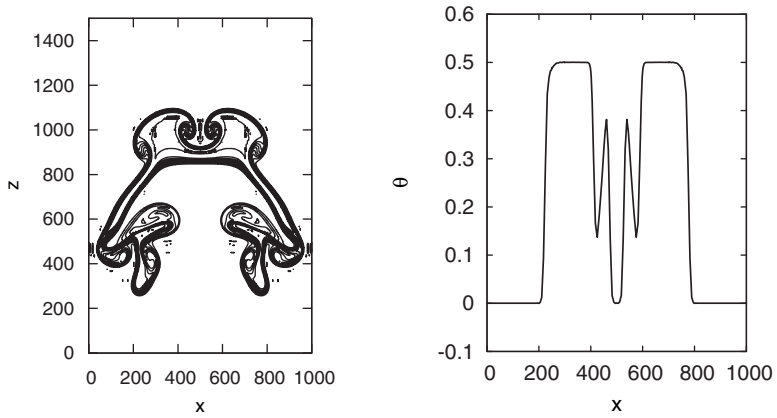

FIG. 6.4. *Nonsmooth bubble test case, potential temperature perturbation at time level* $600\,s$. *Left: contour plot using values between* $0\,K$ *and* $0.52\,K$ *with an interval of* $0.05\,K$. *Right: profile along constant height* $z = 1000\,m$.

conditions are applied, except for the energy balance equation, where the temperature gradient is imposed on bottom and top boundaries to avoid the formation of a thermal boundary layer, as discussed in [31]. The computational domain is $[0\,m, 1000\,m] \times [0\,m, 1500\,m]$ and a grid composed of 20×30, 10^{th}-order elements is adopted, with equivalent resolution $5\,m$. The time-step is $0.08\,s$, yielding $C^{\max} = 19$ and $C_{adv}^{\max} = 0.15$. Figure 6.4 shows the computed potential temperature perturbation after $600\,s$ and the one-dimensional profile along $z = 1000\,m$ for the same quantity. Minimum and maximum values for the computed solution are $(-2.563 \cdot 10^{-5}, 1.418 \cdot 10^{-5})$ for π, $(-2.386\,m/s, 2.386\,m/s)$ for u, $(-3.965\,m/s, 2.450\,m/s)$ for w, and $(-1.370 \cdot 10^{-3}\,K, 5.026 \cdot 10^{-1}\,K)$ for θ. All these results are in good agreement with those obtained for the same problem using the explicit spectral element and DG methods described in [31]. Concerning conservation, for this problem we expect mass to remain constant. This is verified up to machine precision in the numerical simulation, where we observe a relative deviation of $2.555 \cdot 10^{-11}$. In order to verify that the efficiency gain associated with the semi-implicit time discretization are retained

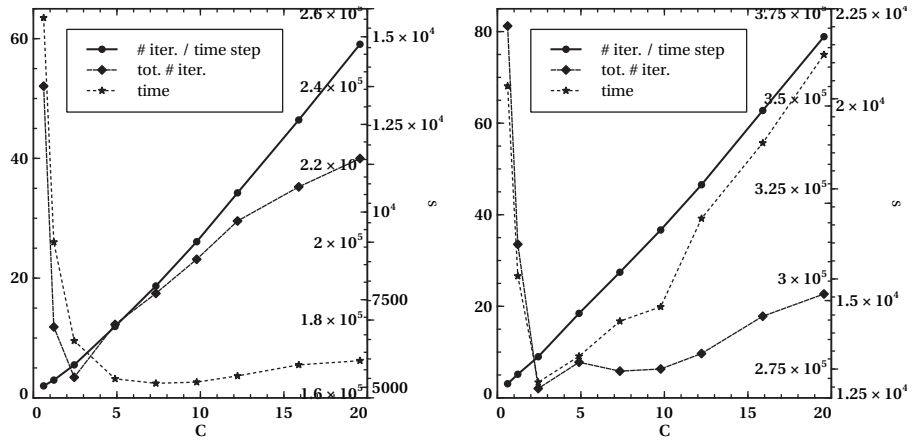

FIG. 6.5. *Nonsmooth bubble test case, number of GMRES iterations per time step (•, left axis), total number of GMRES iterations (♦, first right axis), and total CPU time (★, second right axis) as functions of* $C^{\max}$ *for the case of static condensation (left) and no static condensation (right).*

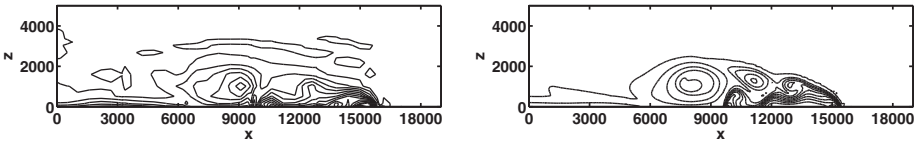

FIG. 6.6. *Density current test case, potential temperature perturbation at time level* $900\,s$ *using* $400\,m$ *(left) and* $100\,m$ *(right) resolution. Contour intervals are* $1\,K$*, with values between* $0\,K$ *and* $-10\,K$*, as in* [51].

in the case of no-flux boundary conditions and nonsmooth solutions, the number of GMRES iterations per time step, the total number of iterations, and the total CPU time are plotted in Figure 6.5 for the case of static condensation (left) and no static condensation (right), for 10×15, 10^{th}-order elements. The total time for the same computation using an explicit BDF method is $2.12 \cdot 10^4\,s$; using the largest Courant number we note in Figure 6.5 that the semi-implicit method with static condensation yields a CPU time of less than $6000\,s$. These results, analogous to those of Figure 6.2, show the robustness of the semi-implicit method.

The fourth test case is the density current test proposed in [51], consisting in a cold bubble placed in a neutral atmosphere. The bubble sinks until hitting the bottom boundary, where no-flux conditions are imposed, and subsequently, Kelvin–Helmholtz rotors develop. Viscosity is prescribed in such a way that a grid-converged solution can be obtained at approximately $50\,m$ resolution. Figure 6.6 shows the computed solution on two grids composed of 8×2 and 32×8, 8^{th}-order elements, respectively, with equivalent resolution $400\,m$ and $100\,m$. Notice that, thanks to the symmetry of the problem, the solution is computed only in half of the domain. The time-steps are $0.8\,s$ and $0.2\,s$, respectively, with $C^{\max} = 2.1$ and $C^{\max}_{adv} = 0.18$. The first case is representative of a poorly resolved flow, since the resolution is too coarse to capture all the features of the grid-converged solution, while the second case is representative of a well-resolved flow. By comparing the results in Figure 6.6 with those in [51], it can be seen that, on the one hand, in the poorly resolved case one of the three rolls present in the reference solution is clearly reproduced, yielding a result which is comparable to the low order *monotonic upstream method* (MUPL) and *piecewise parabolic method*

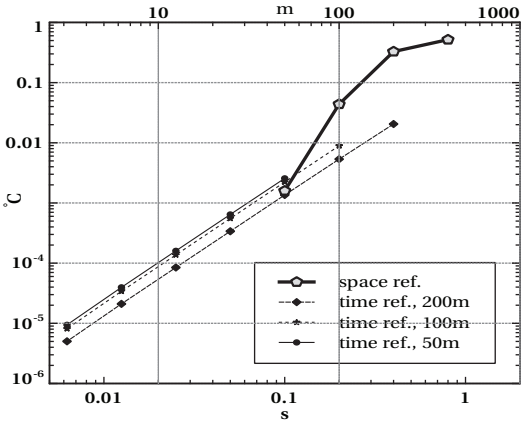

FIG. 6.7. *Self-convergence experiment for the density current test as in* [51], *Figure* 4; L^2 *errors in* $^\circ C$ *for* θ *as functions of the space and time resolutions (axes in* m *and* s, *respectively). The space refinement curve* ($\pentagon$) *is obtained at fixed time step* $\Delta t = 1.5625 \cdot 10^{-3}\, s$, *with a reference solution computed at* $25\, m$ *space resolution. The time refinement curves are computed at fixed space resolution* $200\, m$ ($\blacklozenge$), $100\, m$ ($\bigstar$), *and* $50\, m$ ($\bullet$), *with a reference solution at* $\Delta t = 1.5625 \cdot 10^{-3}\, s$.

(PPM) solutions. This is significant because, on the contrary, the high-order *fully local spectral* (FLS) method, in this case, produces completely meaningless results. On the other hand, in the well-resolved case the solution obtained with the SI-DG formulation is similar to the one obtained with the FLS and close to the grid-converged solution, being, thus, superior to those obtained with the MUPL and PPM schemes. Concerning conservation, we observe a mass relative difference of 4.600×10^{-12} and 1.818×10^{-11} in the coarse and fine resolution cases, respectively. To provide a more quantitative measure of the accuracy of the SI-DG formulation, we carry out a self-convergence study analogous to the one described in section 3 of [51]. For this test, a reference solution at spatial resolution $25\, m$ and $\Delta t = 1.5625 \cdot 10^{-3}\, s$ is used to estimate the separate effects on the error of space and time refinements. The space refinement is obtained by fixing the time step as in the reference solution and considering the four spatial resolutions $400\, m$, $200\, m$, $100\, m$, and $50\, m$, while for the time refinement the spatial resolution is fixed and decreasing time steps are considered, starting from the largest stable time step allowed by the semi-implicit time discretization. The resulting L^2 norm of the error in θ, normalized by the square root of the domain area, is plotted in Figure 6.7, which can be directly compared with Figure 4 of [51]. The choice of the two horizontal axes is such that the point of the time refinement curve at $200\, m$ with $\Delta t = 0.4\, s$, which is the maximum stable time step at this resolution, has the same abscissa as the point at $200\, m$ resolution in the space refinement curve, and so on for the other two time refinement curves. This allows for an immediate comparison of the errors resulting from the time and space discretizations, which can be read from the space refinement curve and the corresponding time refinement curve *at the same abscissa*. Concerning the space refinement curve, we observe that, at coarse resolution, the error of the SI-DG method is smaller than the error reported in [51] by a factor 2, a ratio which reaches a factor 10 at the highest resolution. The experimental convergence rates are 0.66, 2.90, and 4.78, which are consistent with a convergence to the theoretical value 9. Concerning the time refinement curve, we observe the theoretical convergence rate 2. Finally, concerning the ratio between space and time discretization errors, we observe that, for resolutions coarser or equal to

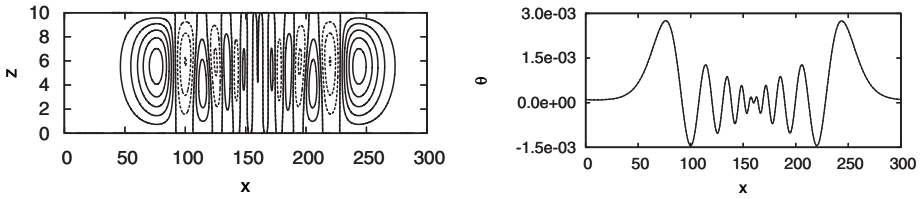

FIG. 6.8. *Inertia-gravity wave test case, potential temperature at time level* $3000\,s$ *(coordinates in km). Left: contour plot with contour values between* $-1.5 \cdot 10^{-3}\,K$ *and* $3 \cdot 10^{-3}\,K$ *with contour interval* $5 \cdot 10^{-4}\,K$ *(negative values: dashed lines). Right: profile along* $5\,km$ *height for the semi-implicit (continuous) and for the explicit (dashed) DG formulations.*

$100\,m$, the time discretization error at the largest stable time step is roughly one order of magnitude smaller than the space discretization error, so that the larger stability of the semi-implicit time integrator can be fully exploited without compromising the quality of the results. The situation is different for the well-resolved case at $50\,m$ resolution, where the time discretization error is larger than the space discretization one. For this case, one should either use a smaller time step or resort to higher order methods, such as BDF3 in Table 3.1.

6.2. Inertia-gravity waves. In this section, we study the nonhydrostatic inertia-gravity wave test proposed in [49]. A background atmosphere is considered with constant Brunt–Väisälä frequency $N = 0.01\,s^{-1}$ and uniform horizontal flow $\overline{u} = 20\,m/s$. The computational domain is $[0\,km, 300\,km] \times [0\,km, 10\,km]$, with no-flux boundary conditions on bottom and top boundaries and periodic conditions on lateral boundaries. The flow is inviscid. The initial condition is represented by a thermal anomaly centered at $(x, z) = (100\,km, 5\,km)$, and the flow is simulated until $T_{fin} = 3000\,s$. A grid composed of 120×4, 10^{th}-order elements is employed, with equivalent resolution $0.25\,km$. The time-step is $1\,s$, yielding $C^{\max} = 5.1$ and $C^{\max}_{adv} = 0.24$. The computed potential temperature θ is shown in Figure 6.8. These results are in good agreement with those presented in [49, 1, 31]. To assess in greater detail the effect of the semi-implicit time discretization, in Figure 6.8, right, the computed profile from [31] with explicit time stepping is also reported. It can be seen that the two curves are nearly coincident. Extrema for the computed solution are $(-7.128 \cdot 10^{-7}, 9.106 \cdot 10^{-7})$ for π, $(-1.061 \cdot 10^{-2}\,m/s, 1.064 \cdot 10^{-2}\,m/s)$ for u, $(-2.402 \cdot 10^{-3}\,m/s, 2.877 \cdot 10^{-3}\,m/s)$ for w, and $(-1.511 \cdot 10^{-3}\,K, 2.806 \cdot 10^{-3}\,K)$ for θ. The corresponding relative differences with respect to the explicit case are 46.9%, 0.56%, 13.4%, and 0.68%, respectively, thus, confirming that the distortion caused by the semi-implicit time discretization for acoustic modes, which is evident in the large pressure difference, does not affect the slow modes. Finally, concerning conservation, we notice that for this problem we expect mass, horizontal momentum, and total energy to remain constant. This is verified up to machine precision in the numerical simulation, where we observe for these three quantities relative errors equal to $1.669 \cdot 10^{-8}$, $2.645 \cdot 10^{-7}$, and $1.640 \cdot 10^{-8}$, respectively.

6.3. Mountain wave simulations. In this section, we study three test cases based on the simulation of hydrostatic and nonhydrostatic mountain waves. Besides assessing the overall accuracy of the proposed numerical scheme, we intend with these tests to verify the robustness of the approach discussed in section 2.1 and section 3 to deal with open-boundary conditions in the framework of a conservative formulation for the flow equations and semi-implicit time integration. All the test cases consider

a uniform horizontal flow impinging over an isolated mountain. The background atmosphere is characterized by constant Brunt–Väisäla frequency; no flux conditions are imposed on the bottom boundary while open-boundary conditions are imposed on lateral and top boundaries. The flow is inviscid in all the test cases. A classical review on mountain waves is [50], while we refer to [36, 24, 40, 7, 46, 29, 28] for a detailed description of the test cases and reference solutions.

For the first test case, we consider an isothermal atmosphere at $\overline{T} = 250K$ and Brunt–Väisäilä frequency $N = 1.95 \cdot 10^{-2}\, s^{-1}$ and a uniform horizontal flow at $\overline{u} = 20\, m/s$. The computational domain is $[0\, km, 240\, km] \times [0\, km, 30\, km]$, and the mountain profile is defined by the *versiera di Agnesi*

$$h_m(x) = \frac{h_{m_0}}{1 + \left(\frac{x - x_c}{a_c}\right)^2}, \tag{6.1}$$

with $h_{m_0} = 1\, m$, $x_c = 120\, km$, and $a_c = 10\, km$. As shown in [50], this choice of parameters results in hydrostatic flow. A grid composed of 20×12, 10^{th}-order elements is adopted, with equivalent resolution $1.2\, km$ in the horizontal and $0.25\, km$ in the vertical. The time-step is $3.5\, s$, yielding $C^{\max} = 18.6$ and $C^{\max}_{adv} = 0.18$. The computed solution at time level $T_{fin} = 10\,$hrs is presented in Figure 6.9. A pseudo-analytic solution computed with Fourier transform techniques is also represented. In addition, Figure 6.11, left, shows the computed vertical flux of horizontal momentum (whose magnitude equals the drag exerted by the flow on the obstacle), at various time levels, normalized by the analytic value

$$M_H = -\frac{\pi_c}{4} \overline{\rho}_s \overline{u} N h^2_{m_0}, \tag{6.2}$$

with $\overline{\rho}_s = \overline{\rho}(0)$ denoting the surface density. In general, an overall agreement of the computed solution with the analytic solution can be observed. The RMS errors are 1.44×10^{-7} for π, $2.61 \times 10^{-3}\, m/s$ for u, $7.44 \times 10^{-5}\, m/s$ for w, and $1.79 \times 10^{-3}\, K$ for θ. Concerning the normalized momentum flux, its value is close to 1 far from the upper boundary, and goes to zero within the damping layer. This fact is in good agreement with the analytic results and also confirms that a steady state configuration, characterized by a uniform momentum flux, is attained.

For the second test case, we consider a constant stability atmosphere with Brunt–Väisäilä frequency $N = 1 \cdot 10^{-2}\, s^{-1}$ and surface temperature $\overline{T}_s = 280\, K$ and a uniform horizontal flow with $\overline{u} = 10\, m/s$. The computational domain is $[0\, km, 144\, km] \times [0\, km, 30\, km]$, and the mountain profile is given by (6.1) with $h_{m_0} = 1\, m$, $x_c = 72\, km$ and $a_c = 1\, km$. This choice of parameters results in nonhydrostatic flow. A grid composed of 40×10, 10^{th}-order elements is adopted, with equivalent resolution $0.36\, km$ in the horizontal and $0.3\, km$ in the vertical. The time-step is $2\, s$, yielding $C^{\max} = 8.39$ and $C^{\max}_{adv} = 0.17$. The computed solution at time level $T_{fin} = 5\,$hrs is presented in Figure 6.10, together with a pseudo-analytic solution. Figure 6.11, right, shows the computed vertical flux of horizontal momentum at various intermediate time levels, normalized by the analytic value

$$M_{NH} = -0.457 \frac{\pi_c}{4} \overline{\rho}_s \overline{u} N h^2_{m_0}.$$

In general, an overall agreement of the computed solution with the analytic solution can be observed, although some incorrect maxima can be seen downstream of the obstacle, which can be possibly ascribed to unphysical reflections in the absorbing layer. The RMS errors are 2.28×10^{-8} for π, $6.98 \times 10^{-4}\, m/s$ for u, $2.59 \times 10^{-4}\, m/s$

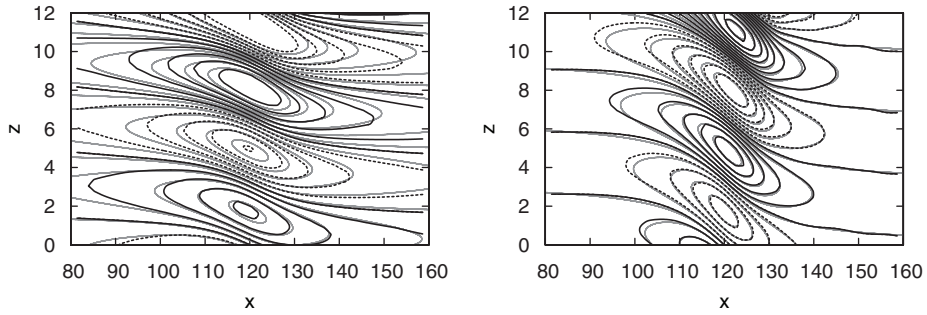

FIG. 6.9. *Linear hydrostatic mountain test case, computed solution at time level* $10\,hrs$ *(black, dashed line for negative values) and analytic steady state solution (gray), coordinates in km. Left: horizontal velocity u with contour lines between* $-2.5 \cdot 10^{-2}\,m/s$ *and* $2.5 \cdot 10^{-2}\,m/s$ *with contour interval* $5 \cdot 10^{-3}\,m/s$*. Right: vertical velocity w with contour lines between* $-5 \cdot 10^{-3}\,m/s$ *and* $5 \cdot 10^{-3}\,m/s$ *with contour interval* $5 \cdot 10^{-4}\,m/s$*.*

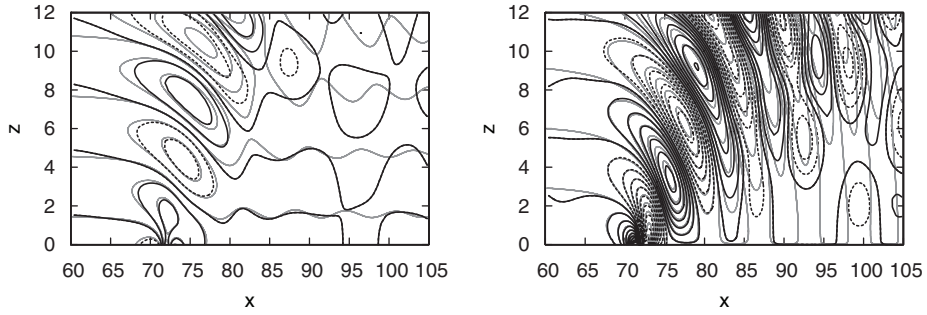

FIG. 6.10. *Linear nonhydrostatic mountain test case, computed solution at time level* $5\,hrs$ *(black, dashed line for negative values) and analytic steady state solution (gray), coordinates in km. Left: horizontal velocity u with contour lines between* $-2.5 \cdot 10^{-2}\,m/s$ *and* $2.5 \cdot 10^{-2}\,m/s$ *with contour interval* $2.5 \cdot 10^{-3}\,m/s$*. Right: vertical velocity w with contour lines between* $-5 \cdot 10^{-3}\,m/s$ *and* $5 \cdot 10^{-3}\,m/s$ *with contour interval* $5 \cdot 10^{-4}\,m/s$*.*

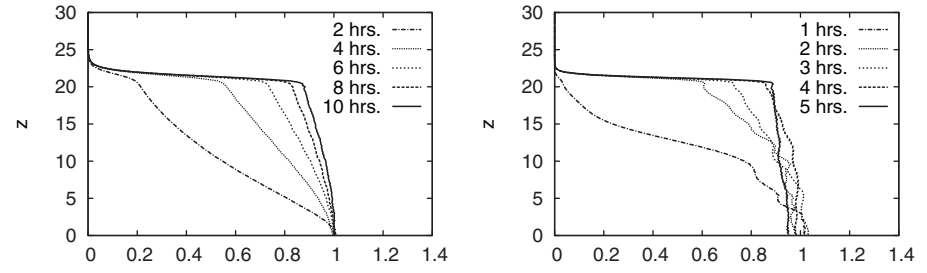

FIG. 6.11. *Mountain wave test cases, normalized vertical flux of horizontal momentum. Left: hydrostatic case, time levels* $2\,hrs$*,* $4\,hrs$*,* $6\,hrs$*,* $8\,hrs$*, and* $10\,hrs$*. Right: nonhydrostatic case, time levels* $1\,hrs$*,* $2\,hrs$*,* $3\,hrs$*,* $4\,hrs$*, and* $5\,hrs$*.*

for w, and $2.50 \times 10^{-4}\,K$ for θ. Concerning the normalized momentum flux, the same considerations as for the previous case apply.

The third mountain test case has been proposed in [46], and various solutions are available in the literature, as for instance, [29, 28]. A uniform stability background atmosphere is considered with Brunt–Väisälä frequency $N = 1 \cdot 10^{-2}\,s^{-1}$, surface

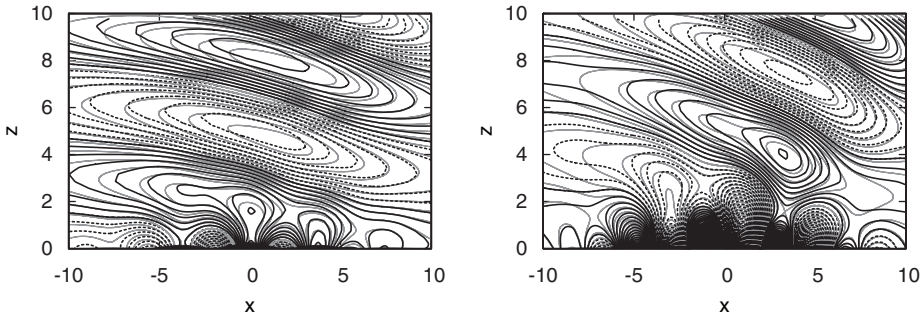

FIG. 6.12. *Schär mountain test case, computed solution at time level* $10\,hrs$ *(black, dashed line for negative values) and linearized analytic steady state solution (gray), coordinates in* km*. Left: horizontal velocity* u *with contour lines between* $-2\,m/s$ *and* $2\,m/s$ *with contour interval* $0.2\,m/s$*. Right: vertical velocity* w *with contour lines between* $-2\,m/s$ *and* $2\,m/s$ *with contour interval* $0.05\,m/s$*.*

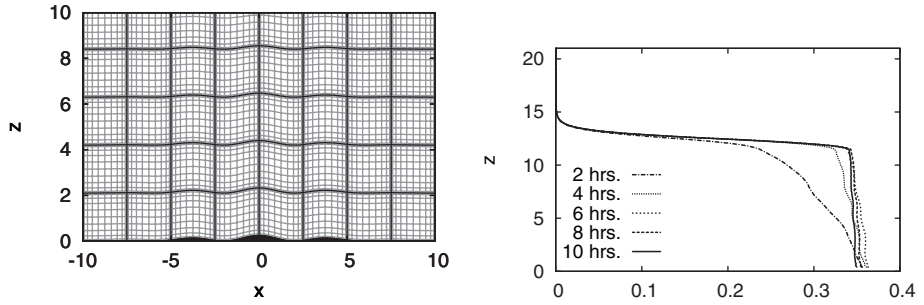

FIG. 6.13. *Schär mountain test cases. Left: computational grid, element boundaries are displayed in black and LGL points are located at the intersections of the gray lines. Right: normalized vertical flux of horizontal momentum at time levels* $2\,hrs$*,* $4\,hrs$*,* $6\,hrs$*,* $8\,hrs$*, and* $10\,hrs$*.*

temperature $\overline{T}_s = 280\,K$, and a uniform horizontal flow with $\overline{u} = 10\,m/s$. The computational domain is $[-25\,km, 25\,km] \times [0\,km, 21\,km]$, and the mountain profile is

$$h_m(x) = h_{m_0} e^{-\left(\frac{x}{a_c}\right)^2} \cos^2\left(\frac{\pi_c x}{\lambda_c}\right)$$

with $h_{m_0} = 250\,m$, $a_c = 5\,km$, and $\lambda_c = 4\,km$. As pointed out in [46], the orography profile forces two distinct types of internal waves: a large-scale hydrostatic wave characterized by deep vertical propagation and a smaller-scale, nonhydrostatic wave characterized by rapid decay with height. A grid composed of 20×10, 10^{th}-order elements is adopted, with equivalent resolution $0.25\,km$ in the horizontal and $0.21\,km$ in the vertical. The time-step is $1.4\,s$, yielding $C^{\max} = 8.40$ and $C^{\max}_{adv} = 0.20$. The computed solution at time level $T_{fin} = 10\,\text{hrs}$ is presented in Figure 6.12, together with a pseudo-analytic linear solution. Notice, however, that due to the nonnegligible height of the mountain, the linear solution should be taken as a qualitative reference rather than the "truth". A good agreement of the numerical solution is observed both with the analytic linear solution and with results in the literature. In particular, notice that the numerical solution correctly reproduces the different vertical structures of the two superimposed waves, with the small-scale perturbation exhibiting the correct decay with height. The RMS errors are 7.93×10^{-6} for π, $1.87 \times 10^{-1}\,m/s$ for u, $3.86 \times 10^{-2}\,m/s$ for w, and $4.41 \times 10^{-2}\,K$ for θ. Figure 6.13 shows a detail of the computational grid, left, and the computed vertical flux of horizontal momentum at

various intermediate time levels, normalized by the analytic value for the hydrostatic case (6.2), right. The momentum flux is constant along the vertical, indicating that a steady state configuration is reached, and a value different from one is explained by the different shape of the mountain with respect to the previous test.

7. Conclusions. In the present article we have proposed a formulation in which the SI time integration strategy is adopted in the context of a high-order DG spatial discretization for the solution of the nonhydrostatic, compressible Navier–Stokes equation for atmospheric flows. The main reason for investigating this combination is the increase of the efficiency of the DG method when applied to mesoscale flows, and, more in general, to low Mach number compressible flows. A critical step in a SI formulation is represented by the solution of the linear system for the implicit part of the scheme. We have shown that it is possible to reformulate such a problem in terms of a pseudo-Helmholtz operator, and that the resulting discretization fits into the LDG framework for elliptic problems. We have also described how to sidestep some well-known difficulties in dealing with penalization terms in the numerical fluxes by exploiting the LGL numerical quadrature. The potential benefits of this approach have then been demonstrated with some classical numerical tests. In the future, we plan to implement the pseudo-Helmholtz form of the linear system for the case of general boundary conditions, develop high-order semi-implicit methods with adaptive time-stepping, explore alternative high-order non-reflective boundary conditions, and extend the model to three dimensions to investigate the effects of rotation. A further possible extension is represented by the introduction of the semi-Lagrangian DG method proposed in [41] to deal with the stability limit associated with advection.

Acknowledgments. The work of the first author (MR) was mainly done while he was a Ph.D. student at "Dipartimento di Matematica F. Brioschi, Politecnico di Milano", under the supervision of Riccardo Sacco and Luca Bonaventura, whom he wishes to thank for several discussions which greatly improved the present manuscript.

REFERENCES

[1] N. Ahmad and J. Lindeman, *Euler solutions using flux–based wave decomposition*, Int. J. Numer. Methods Fl., 54 (2007), pp. 47–72.

[2] V. Aizinger and C. Dawson, *A discontinuous Galerkin method for two-dimensional flow and transport in shallow water*, Adv. Water Resour., 25 (2002), pp. 67–84.

[3] D. Arnold, F. Brezzi, B. Cockburn, and L. Marini, *Unified analysis of discontinuous Galerkin methods for elliptic problems*, SIAM J. Numer. Anal., 39 (2002), pp. 1749–1779.

[4] D. Arnold and F. Brezzi, *Mixed and nonconforming finite–element methods - implementation, postprocessing and error-estimates*, RAIRO - Math. Model. Num., 19 (1985), pp. 7–32.

[5] F. Bassi and S. Rebay, *A high-order accurate discontinuous finite element method for the numerical solution of the compressible Navier–Stokes equations*, J. Comput. Phys., 131 (1997), pp. 267–279.

[6] F. Bassi and S. Rebay, *High-order accurate discontinuous finite element solution of the* 2*D Euler Equations*, J. Comput. Phys., 138 (1997), pp. 251–285.

[7] L. Bonaventura, *A semi-implicit semi-Lagrangian scheme using the height coordinate for a nonhydrostatic and fully elastic model of atmospheric flows*, J. Comput. Phys., 158 (2000), pp. 186–213.

[8] N. Botta, R. Klein, S. Langenberg, and S. Lützenkirchen, *Well balanced finite volume methods for nearly hydrostatic flows*, J. Comput. Phys., 196 (2004), pp. 539–565.

[9] J. Boyd, *Chebyshev and Fourier Spectral Methods*, Dover Publications Inc., Mineola, New York, 2001.

[10] D. Burridge, *A split semi-implict reformulation of the Bushby–Timpson* 10*-level model*, Q. J. R. Meteorol. Soc., 101 (1975), pp. 777–792.

[11] C. Canuto, M. Hussaini, A. Quarteroni, and T. Zang, *Spectral Methods*, Springer, Berlin, 2006.
[12] R. Carpenter, K. Droegemeier, P. Woodward, and C. Hane, *Application of the piecewise parabolic method (PPM) to meteorological modeling*, Mon. Wea. Rev., 118 (1990), pp. 586–612.
[13] P. Castillo, B. Cockburn, I. Perugia, and D. Schötzau, *An a priori error analysis of the local discontinuous Galerkin method for elliptic problems*, SIAM J. Numer. Anal., 38 (2000), pp. 1676–1706.
[14] B. Cockburn, B. Dong, J. Guzmán, M. Restelli, and R. Sacco, *A hybridizable discontinuous Galerkin method for steady state convection-diffusion-reaction problems*, SIAM J. Sci. Comput., submitted (2008).
[15] B. Cockburn, B. Dong, and J. Guzmán, *A superconvergent LDG-hybridizable Galerkin method for second-order elliptic problems*, Math. Comput., 77 (2008), pp. 1887–1916.
[16] B. Cockburn, C. Johnson, C. Shu, and E. Tadmor, *Advanced Numerical Approximation of Nonlinear Hyperbolic Equations*, Springer, Berlin, 1997.
[17] B. Cockburn and C. Shu, *The local discontinuous Galerkin method for time-dependent convection-diffusion systems*, SIAM J. Numer. Anal., 35 (1998), pp. 2440–2463.
[18] M. J. P. Cullen, *A test of a semi-implicit integration technique for a fully compressible nonhydrostatic model*, Q. J. R. Meteorol. Soc., 116 (1990), pp. 1253–1258.
[19] C. Dawson and V. Aizinger, *A discontinuous Galerkin method for three-dimensional shallow water equations*, J. Sci. Comput., 22–23 (2005), pp. 245–267.
[20] J. Dea, F. Giraldo, and B. Neta, *High–order Higdon non–reflecting boundary conditions for the linearized Euler equations*, NPS Technical report NPS-MA-07-001, Naval Postgraduate School, Monterey, CA, Apr. 2007.
[21] J. Dea, F. Giraldo, and B. Neta, *High-order Higdon non-reflecting boundary conditions for the linearized 2-D Euler equations: No mean flow case*, Wave Motion (2008), doi:10.1016/j.wavemoti.2008,11.002.
[22] J. Dea, *High-order non–reflecting boundary conditions for the linearized Euler equations*, Ph.D. thesis, Naval Postgraduate School, 2008.
[23] V. Dolejší and M. Feistauer, *A semi-implicit discontinuous Galerkin finite element method for the numerical solution of inviscid compressible flow*, J. Comput. Phys., 198 (2004), pp. 727–746.
[24] D. Durran and J. Klemp, *A compressible model for the simulation of moist mountain waves*, Mon. Wea. Rev., 111 (1983), pp. 2341–2361.
[25] D. Durran, *Numerical Methods for Wave Equations in Geophysical Fluid Dynamics*, Springer-Verlag, New York, 1999.
[26] M. Feistauer, V. Dolejší, and V. Kučera, *On the discontinuous Galerkin method for the simulation of compressible flow with wide range of Mach numbers*, Comput. Vis. Sci., 10 (2007), pp. 17–27.
[27] M. Feistauer and V. Kučera, *On a robust discontinuous Galerkin technique for the solution of compressible flow*, J. Comput. Phys., 224 (2007), pp. 208–221.
[28] A. Gassmann and H. Herzog, *A consistent time–split numerical scheme applied to the nonhydrostatic compressible equations*, Mon. Wea. Rev., 135 (2007), pp. 20–36.
[29] A. Gassmann, *An improved two-time-level split-explicit integration scheme for non-hydrostatic compressible models*, Meteorol. Atmos. Phys., 88 (2005), pp. 23–38.
[30] F. Giraldo, J. Hesthaven, and T. Warburton, *Nodal high-order discontinuous Galerkin methods for the spherical shallow water equations*, J. Comput. Phys., 181 (2002), pp. 499–525.
[31] F. Giraldo and M. Restelli, *A study of spectral element and discontinuous Galerkin methods for the Navier–Stokes equations in nonhydrostatic mesoscale atmospheric modeling: Equation sets and test cases*, J. Comput. Phys., 227 (2008), pp. 3849–3877.
[32] F. Giraldo and T. Warburton, *A high-order triangular discontinuous Galerkin oceanic shallow water model*, Int. J. Numer. Methods Fl., 56 (2008), pp. 899–925.
[33] F. Giraldo, *Semi-implicit time-integrators for a scalable spectral element atmospheric model*, Q. J. R. Meteorol. Soc., 131 (2005), pp. 2431–2454.
[34] F. Giraldo, *High-order triangle-based discontinuous Galerkin methods for hyperbolic equations on a rotating sphere*, J. Comput. Phys., 214 (2006), pp. 447–465.
[35] G. Karniadakis, M. Israeli, and S. Orszag, *High–order splitting methods for the incompressible Navier–Stokes equations*, J. Comput. Phys., 97 (1991), pp. 414–443.
[36] J. Klemp and D. Lilly, *Numerical simulation of hydrostatic mountain waves*, J. Atmos. Sci., 35 (1978), pp. 78–107.
[37] J. Klemp, W. Skamarock, and J. Dudhia, *Conservative split-explicit time integration methods for the compressible nonhydrostatic equations*, Mon. Wea. Rev., 135 (2007), pp. 2897–2913.

[38] M. Kwizak and A. Robert, *A semi-implicit scheme for grid point atmospheric models of the primitive equations*, Mon. Wea. Rev., 99 (1971), pp. 32–36.
[39] R. Nair, S. Thomas, and R. Loft, *A discontinuous Galerkin global shallow water model*, Mon. Wea. Rev., 133 (2005), pp. 876–888.
[40] J. Pinty, R. Benoit, E. Richard, and R. Laprise, *Simple tests of a semi-implicit semi-Lagrangian model on 2D mountain wave problems*, Mon. Wea. Rev., 123 (1995), pp. 3042–3058.
[41] M. Restelli, L. Bonaventura, and R. Sacco, *A semi-Lagrangian discontinuous Galerkin method for scalar advection by incompressible flows*, J. Comput. Phys., 216 (2006), pp. 195–215.
[42] M. Restelli, *Semi–Lagrangian and semi–implicit discontinuous Galerkin methods for atmospheric modeling applications*, Ph.D. Thesis, Politecnico di Milano, 2007.
[43] H. Ritchie, C. Temperton, A. Simmons, M. Hortal, T. Davies, D. Dent, and M. Hamrud, *Implementation of the semi-Lagrangian method in a high-resolution version of the ECMWF forecast model*, Mon. Wea. Rev., 123 (1995), pp. 489–514.
[44] A. Robert, *Bubble convection experiments with a semi-implicit formulation of the Euler equations*, J. Atmos. Sci., 50 (1993), pp. 1865–1873.
[45] V. Rusanov, *Calculation of interaction of non–steady shock waves with obstacles*, USSR Comp. Math, and Math. Phys., 1 (1961), pp. 267–279.
[46] C. Schär, D. Leuenberger, O. Fuhrer, D. Lüthi, and C. Girard, *A new terrain-following vertical coordinate formulation for atmospheric prediction models*, Mon. Wea. Rev., 130 (2002), pp. 2459–2480.
[47] D. Schwanenberg and J. Köngeter, *A discontinuous Galerkin method for the shallow water equations with source terms*, in Discontinuous Galerkin Methods, Springer, Berlin, 2000, pp. 419–424.
[48] A. Simmons, B. Hoskins, and D. Burridge, *Stability of the semi-implicit method of time integration*, Mon. Wea. Rev., 106 (1978), pp. 405–412.
[49] W. Skamarock and J. Klemp, *Efficiency and accuracy of the Klemp–Wilhelmson time-splitting technique*, Mon. Wea. Rev., 122 (1994), pp. 2623–2630.
[50] R. Smith, *The influence of mountains on the atmosphere*, Adv. Geophys., 21 (1979), pp. 87–230.
[51] J. Straka, R. Wilhelmson, L. Wicker, J. Anderson, and K. Droegemeier, *Numerical solutions of a non–linear density current: A benchmark solution and comparisons*, Int. J. Numer. Methods Fl., 17 (1993), pp. 1–22.
[52] M. Tanguay, A. Robert, and R. Laprise, *A semi-implicit semi-Lagrangian fully compressible regional forecast model*, Mon. Wea. Rev., 118 (1990), pp. 1970–1980.
[53] M. Tapp and P. White, *A non-hydrostatic mesoscale model*, Q. J. R. Meteorol. Soc., 102 (1976), pp. 277–296.
[54] E. Toro, *Riemann solvers and numerical methods for fluid dynamics*, Springer–Verlag, Berlin, Heidelberg, 1997.
[55] Y. Xia, Y. Xu, and C. Shu, *Efficient time discretization for local discontinuous Galerkin methods*, Discrete Contin. Dyn. Syst. Ser. B, 8 (2007), pp. 677–693.
[56] Y. Xu and C. Shu, *Local discontinuous Galerkin methods for three classes of nonlinear wave equations*, J. Comput. Math., 22 (2004), pp. 250–274.